Unstructured grid modelling of offshore wind farm impacts on seasonally stratified shelf seas

Pierre William Cazenave[a,*], Ricardo Torres[a], J. Icarus Allen[a]

[a] *Plymouth Marine Laboratory, Prospect Place, The Hoe, Plymouth, PL1 3DH, United Kingdom*

Abstract

Shelf seas comprise approximately 7% of the world's oceans and host enormous economic activity. Development of energy installations (e.g. Offshore Wind Farms (OWFs), tidal turbines) in response to increased demand for renewable energy requires a careful analysis of potential impacts. Recent remote sensing observations have identified kilometre-scale impacts from OWFs. Existing modelling evaluating monopile impacts has fallen into two camps: small-scale models with individually resolved turbines looking at local effects; and large-scale analyses but with sub-grid scale turbine parameterisations. This work straddles both scales through a 3D unstructured grid model (FVCOM): wind turbine monopiles in the eastern Irish Sea are explicitly described in the grid whilst the overall grid domain covers the south-western UK shelf. Localised regions of decreased velocity extend up to 250 times the monopile diameter away from the monopile. Shelf-wide, the amplitude of the M_2 tidal constituent increases by up to 7%. The turbines enhance localised vertical mixing which decreases seasonal stratification. The spatial extent of this extends well beyond the turbines into the surrounding seas. With significant expansion of OWFs on continental shelves, this work highlights the importance of how OWFs may impact coastal (e.g. increased flooding risk) and offshore (e.g. stratification and nutrient cycling) areas.

Keywords: offshore wind farm, wind turbines, monopile, FVCOM, unstructured grid, stratification

1. Introduction

Shelf seas comprise approximately 7% of the world's oceans and are the focus of an enormous amount of economic activity. They have been the subject of intensive study for the last century during which time their dynamics have been well documented (e.g. Proudman and Doodson, 1924; Doodson and Corkan, 1933; Cloet, 1954; Simpson and Hunter, 1974; Pingree and Maddock, 1977; Pingree et al., 1982). Shelf seas are dynamic environments subject seasonal heating, atmospheric fluxes, tides, river inputs and open ocean exchange (Holt et al., 2012). They are characterised by seasonal temperature stratification in which summer heating is able to stratify the water column and overcome strong tidal mixing (Holt and Umlauf, 2008). Stratified regions are characterised by a sharp seasonal thermocline (developed with the onset of positive net heat flux into the water (Smyth et al., 2014)) whilst non-stratified regions are dominated by tidal mixing and remain vertically homogeneous year round. Tidal mixing fronts form at the interface between these stratified regions and shallower non-stratified waters (Simpson and Hunter, 1974).

Shelf seas are critical in maintaining a complex ecosystem (Proctor et al., 2003; Holt et al., 2012; Wakelin et al., 2012) which has been shown to modulate the impacts of climatic variability (Barange et al., 2011; Artioli et al., 2012). The behaviour of the shelf sea ecosystem is predominantly controlled by the timing and rate of water transport from low light and nutrient rich deep waters into high light nutrient poor surface waters (Pingree et al., 1982; Richardson et al., 2000). Tidal mixing

*Corresponding author. Tel.: +44 (0)1752 633100
Email addresses: pica@pml.ac.uk (Pierre William Cazenave), rito@pml.ac.uk (Ricardo Torres), jia@pml.ac.uk (J. Icarus Allen)

fronts separate the nutrient-rich from nutrient-poor waters, thus their location, stability and strength are critical in the evolution of many ecosystem processes (e.g. spring bloom phenology and magnitude). Furthermore, the interplay between density gradients and tidal currents generates temporally varying Strain-Induced Periodic Stratification (SIPS) which in turn feeds back and modifies the water column structure and tidal ellipses (Simpson et al., 1990; Palmer, 2010). Therefore processes which act to modify either density or currents have the potential to modify the magnitude and timing of SIPS (Souza and Simpson, 1996; Palmer, 2010).

Within the north-western European shelf seas, the UK government's commitment to Offshore Wind Farms (OWFs) is considerable: as of 2008, the UK has installed OWFs with a combined 3.7GW capacity; the UK could be committed to delivering 22.4% (29GW) of its total electricity generation (129GW) from OWFs under the EU 2020 Renewable Energy Targets (Carbon Trust, 2008). This massive UK investment in OWFs is under way with 1,183 offshore wind turbines already installed. However, despite the rapid introduction of large-scale OWFs to the UK's shelf seas, the potential impacts these devices have on shelf sea hydrodynamics remain relatively unknown. This is due largely to the cost and complexity of observational campaigns capable of capturing the potential impacts. Recent analyses of remote sensing data have observed impacts derived from the introduction of offshore wind turbines several kilometres from their siting (Li et al., 2014; Vanhellemont and Ruddick, 2014), thus, large-scale work to quantify these impacts is needed.

The majority of the work to date has been of i) small-scale models with explicit individual turbines (Roulund et al., 2005; Jensen et al., 2006; Okorie, 2011) and ii) large-scale model domains with turbine impacts parameterised as sub-grid scale processes through increased bed roughness (Lambkin et al., 2009), water column velocity (Shapiro, 2011), turbulence models (Rennau et al., 2012) or Linear Momentum Actuator Disk Theory (LMADT) (Serhadlıoğlu et al., 2013). Parameterisation is computationally efficient, however, it omits small-scale turbulent processes which can have important impacts for horizontal and vertical water structure (Christie et al., 2012).

van der Molen et al. (2014) investigated the impact of wind farm geometry with a total of 4,800 turbines spread over 40 wind farms through a coupled physical-ecosystem model (GETM-ERSEM-BFM) as well as with the Simulating WAves Nearshore (SWAN) wave model. The wind turbines and their impacts were represented in GETM through a 10% decrease in surface wind speed and in SWAN as 100m dry grid points. The modelling found the turbines increased net primary productivity, though the authors speculate that explicitly including individual turbines in GETM-ERSEM-BFM might increase turbulence and negate this. Modelling of wind turbines in the Baltic Sea by Rennau et al. (2012) found a small effect from turbines represented as 25 and 50m dry elements (results were scaled linearly by factors of 5 and 10 to represent turbines of 5m diameter, an approach which is likely to yield overestimates of the impacts). A number of models have assessed impacts from tidal turbines (i.e. submerged structures) using momentum sink parameterisations (e.g. Yang et al., 2013, 2014) and have shown that, in macrotidal estuaries (e.g. South Puget Sound), such as are common on the UK continental shelf, tidal stream turbine wakes extend approximately 1.5km (Yang et al., 2014). A 2D TELEMAC model was used to investigate a proposed wind farm off the east coast of Ireland (the Dublin Array) (MRG Consulting Engineers Limited, 2013). The model domain covered 2,800km^2 and contained 100,000 elements with 145 turbine monopiles represented as 5m diameter hexagonal islands. The results indicated that horizontal impacts from the wind turbine monopiles reduced surface current speeds by 5% of the maximum at distances of up to thirty times the monopile diameter (MRG Consulting Engineers Limited, 2013). Given the 2D nature of the model, no assessment of the change in vertical velocity, temperature and salinity structure was possible.

The two scales adopted in the approaches to date (spatially limited and high resolution and vice versa) suffer from limitations of scaling: high resolution models are unable to determine whether impacts propagate to distances beyond each model domain; coarse models cannot resolve the small-scale impacts and their potentially important role. One approach to resolving this conundrum is to nest model grids. This, however, often means a one way exchange of information which limits the export of impacts from the small grids to the larger ones, a process which can have important effects on the model results (Zhou et al., 2014). To resolve this, a model must seamlessly resolve and communicate processes across a range of scales, and an unstructured model provides this ability (Jones and Davies, 2007a).

The work presented here expands on existing work by bridging the required scales and extends the approach into the vertical to address implications for stratified shelf seas. The modelling focuses on the impacts generated by the addition of turbine monopiles to the UK shelf, with an emphasis on the eastern Irish Sea (Fig. 1). The UK shelf is tidally dominated (tidal ranges reach 14m in the Bristol Channel), seasonally stratified (onset in April, dissipation in August) shelf sea. Typical surface temperatures are between 3 and 20°C and salinities vary strongly with proximity to river mouths (where they approach zero), but are typically 35.5PSU further offshore. Current speeds rarely exceed $2\,\mathrm{m\,s^{-1}}$, although localised current speeds can exceed $3\,\mathrm{m\,s^{-1}}$ e.g. in the Pentland Firth, Scotland (Martin-Short et al., 2015).

To assess the performance of the Finite Volume Community Ocean Model (FVCOM) at such small scales, a grid sensitivity analysis is performed where inputs are comparable to the conditions in the vicinity of the OWFs in the eastern Irish Sea. The flume analysis is used to guide the development of a shelf configuration, balancing computational resource required against quality of the result. The performance of the shelf model is compared to observed data to validate the hydrodynamics. The main results are an inter-comparison of two model runs in which the wind turbines are included and excluded. The differences in the two model configurations are considered in terms of the horizontal and vertical impacts on the structure of the water column in both the near- and far-field. Finally, the implications of the impacts in terms of considerations for future OWF developments are discussed.

2. Model set up

The Finite Volume Community Ocean Model (FVCOM) is a prognostic, unstructured-grid, finite-volume, free-surface, 3D primitive equation coastal ocean circulation model (Chen et al., 2003). FVCOM solves the 3D momentum, continuity, temperature, salinity and density equations by computing fluxes between unstructured triangular elements. Vertical turbulent mixing is modelled with the General Ocean Turbulence Model (GOTM) using a k-ϵ formulation (Umlauf and Burchard, 2005) whilst horizontal mixing is parameterised through the Smagorinsky scheme (Smagorinsky, 1963). The vertical grid in FVCOM is described in terrain following (sigma) coordinates where shallower areas resolve vertical structure with finer detail.

FVCOM has been widely used in shelf and coastal domains for a range of problems where a strong need exists to resolve varying horizontal scales, including: physical modelling of temperature and salinity stratification (Chen et al., 2007; Yang and Khangaonkar, 2008; Huang, 2011; Zheng and Weisberg, 2012); tracer evolution in complex estuaries (Torres and Uncles, 2011); the relationship between hydrodynamics and pursuit diving bird behaviour (Waggitt et al., 2016a,b); the behaviour of sequestered CO_2 leak plumes (Blackford et al., 2013); and tracking the dispersal of lice (Adams et al., 2012, 2014).

3. Grid sensitivity analysis

3.1. Flume grids

The inclusion of wind turbine monopiles must be analysed in terms of the impact the model grid resolution has on the calculated results. To that end, three

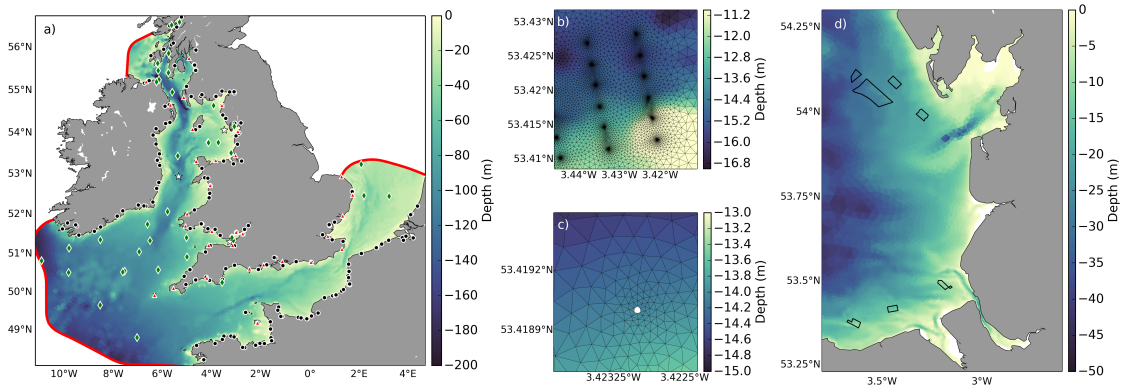

Figure 1: The model domain and bathymetry (a) covering 357,000km^2, where red lines indicate the model open boundaries, the black dots indicate the river input nodes, the red triangles the coastal gauge locations from the NTSLF, the green diamonds the BODC offshore pressure sensor time series and the three white stars the locations of the samples plotted in Fig. 6. The zoomed sections show the grid around multiple turbines (b) and around a single turbine monopile (c). The panel on the right (d) shows the location of the wind farms included in the fine model grid.

flume configurations of FVCOM are used to simulate the flow past a single wind turbine monopile (Fig. 2). The flume is 3×1km in size and all three configurations have a 5m diameter turbine 1km from the left boundary. The turbine is represented as 5m diameter hexagonal island (i.e. infinitely high walls) to best capture the shape of the monopile whilst minimising the number of elements required to represent it. The grid resolutions decrease from 2.5m at the monopile and change linearly with distance to 20m, 10m and 2.5m over a radius of 150m for the low (3,683 nodes), medium (6,869 nodes) and high (27,541 nodes) resolution grids, respectively.

The flume configurations all feature identical forcing, with a constant bed roughness (z_0) of 0.03m, a sinusoidal 3.5m amplitude surface elevation input with the M_2 tidal constituent period (12 hours 25 minutes) at the left open boundary and an implicit open boundary condition (Blumberg and Kantha, 1985) at the right open boundary. The implicit open boundary includes a sponge layer weighted from 0.05 at the open boundary to zero 500m inside the domain to filter high frequency numerical noise due to wave energy reflected back into the model domain (Chen et al., 2013). The water column temperature and salinity are warmer and fresher (12.5°C and 33.5PSU, respectively) in the top 5m of water than the remaining 25m, where temperature and salinity are 11°C and 33.8PSU, respectively. There is no wind, heating, precipitation or air pressure forcing.

3.2. *Results*

Fig. 3 shows the surface current speed anomaly, that is the spatially averaged minus the local current speed (left column), and a vertical transect through the vertical velocity (right column) for the three grids tested after 38 hours of model run time.

The wakes in all three grids from the surface current speed anomaly (Fig. 3a, c and e) are similarly expressed, extending up to 350m from the monopile, beyond which anomalies are outside the range ±0.01m s^{-1}. Detail in the vicinity of the monopile increases with grid resolution, but the general pattern from the high resolution grid is present in the two lower resolution grids: the upstream region of the flow field sees negative velocity anomalies; the velocity anomaly magnitudes increase at 225 and 315° from the monopile and then immediately north and south of the monopile a region of negative anomaly similar in magnitude to the upstream anomaly is visible. The strongest anomalies are upstream and downstream of the monopile, and here the differences between the high, medium and low resolution grids are most evident. The high resolution grid shows an intense 30m wide wake 200m from the monopile whereafter its intensity decreases; the medium and coarse grids show wakes 50m wide with lower intensity at the same

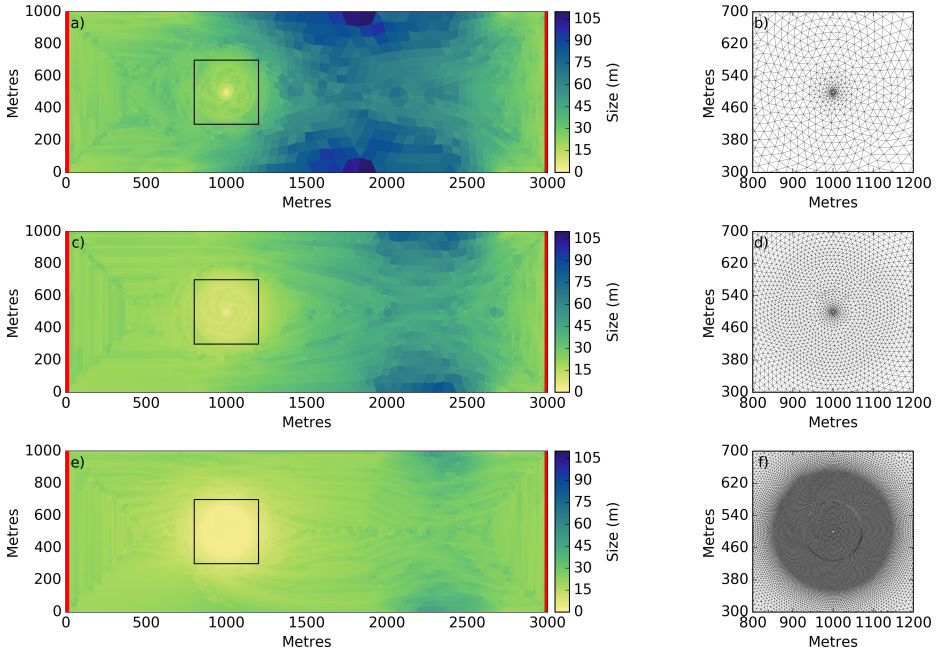

Figure 2: The 3×1km flume model grids with a 5m diameter monopile. Grid resolutions vary from 2.5m at the monopile and change linearly with distance to 20m (a and b), 10m (c and d) and 2.5m (e and f) over a radius of 150m from the monopile. Black boxes indicate the extents of the subset plots in the right hand column. Red lines indicate the location of the open boundaries.

distance. Furthermore, the upstream and downstream anomalies extend further from the monopile in the high resolution grid, whilst the low and medium resolution grid wakes dissipate more rapidly to background values.

The vertical velocity results (Fig. 3b, d and f) also show a similar pattern with some notable differences. All three model results show the same structure: a downward flow upstream of the monopile with upward flow downstream. The vertical distribution of the vertical velocity is also similar across the three grids: the strongest vertical velocity is in the lower part of the water column (from 10m depth to the seabed).

Differences between the three grids appear mainly in the downstream vertical velocity structure and the width of the region over which the vertical velocity is affected by the monopile. The high resolution grid shows greater detail in the vertical velocity structure due to better resolution of the unsteady flow that characterises the wake downstream of the monopile. The eddies that form as the wake becomes unstable have associated vertical velocities (Fig. 3f) that are not resolved in the coarser domains (Fig. 3b and d). Furthermore, the downstream vertical velocity fields are an order of magnitude smaller than those adjacent to the monopole.

The width of the affected region in the immediate vicinity of the monopile is also dependent on the grid resolution: the high resolution grid shows a region over which vertical velocities deviate from the background values is 3–4 times narrower than the equivalent region in the low and medium resolution grids. In addition to its spatial extent, the magnitude is also tied to the resolution, with the high resolution grid showing vertical velocity magnitudes of $0.1\,\mathrm{m\,s^{-1}}$ (Fig. 3f) compared with value of $0.05\,\mathrm{m\,s^{-1}}$ from the low and medium results (Figs. 3b and 3d, respectively).

To assess the impact the grid resolution has on the behaviour of the wake in response to the monopile, three diagnostic variables are calculated from each set of model runs. These have been chosen to represent aspects of the anticipated changes: the current speed anomaly to assess the capture of the wake detail; Turbulent Kinetic Energy (TKE) for the impact on

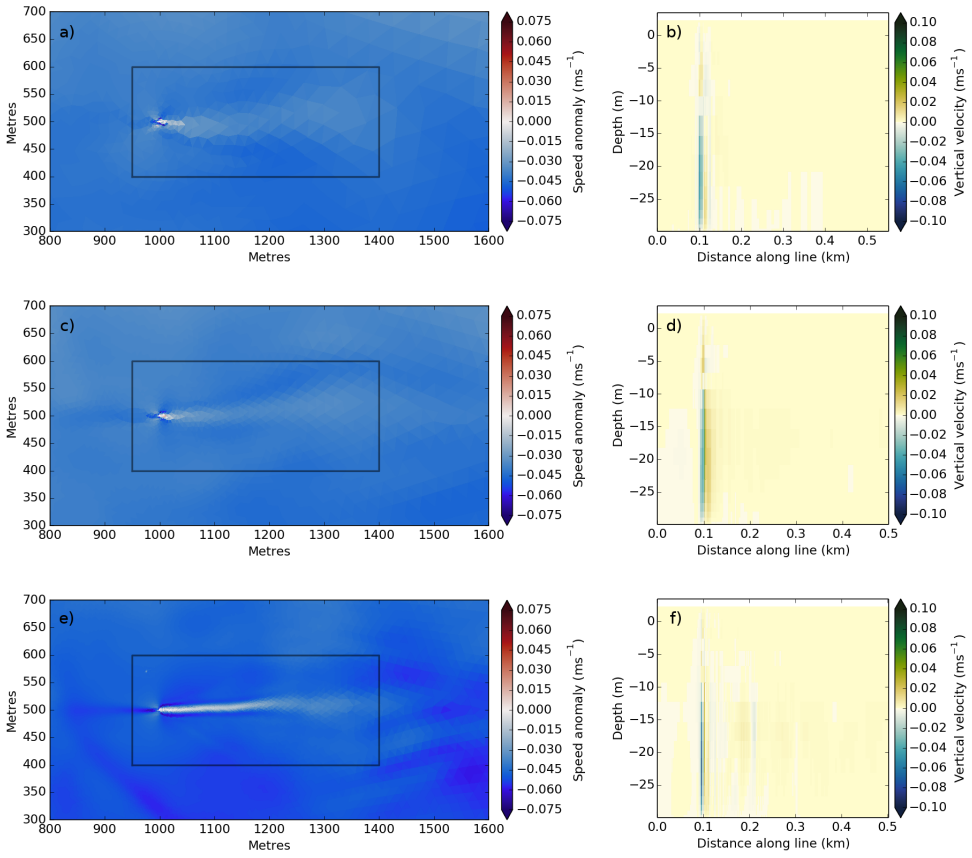

Figure 3: Surface speed anomaly and vertical velocity vertical transects from the low (a and b), medium (c and d) and high (e and f) resolution flume grids. Flow is 0.1cm s^{-1} from the left. The boxes in a, c and e indicate the region over which the variables in Tab. 1 are calculated.

the sub-grid scale turbulence parameterisation; and the potential energy anomaly as a measure of stratification. The potential energy anomaly (ϕ) in J m^{-3} is defined as:

$$\phi = -\frac{g}{h}\int_{z=-h}^{0}(\rho - \hat{\rho})dz \quad (1)$$

where g is the acceleration due to gravity (9.81m s^{-2}), h is the water depth (m), ρ is the density (kg m^{-3}) and $\hat{\rho}$ is the depth-averaged density:

$$\hat{\rho} = \frac{1}{h}\int_{z=-h}^{0}\rho dz \quad (2)$$

Table 1 shows each variable integrated over a horizontal extent which encompasses the wake region (black boxes in Figs. 3a, c and e) and with depth, if appropriate.

The grid sensitivity variables in Table 1 show that the low and medium grids have a very similar response to the monopile across all three measured parameters. The high resolution grid, in contrast, shows differences from the other two grids: in the potential energy anomaly and speed anomaly, the high resolution grid shows values are 80% and 65% of the equivalent values from the low resolution grid, respectively. Thus, the results from the low resolution flume grid are an overestimate of the stratification indicating an underestimate of the vertical mixing and therefore an underestimate of the monopile impact.

In the speed anomaly results, the low grid is overestimating the horizontal velocity signature within the wake region which, again, indicates the wake is not as well resolved (the region of low velocity is less well defined in the lower resolution grids). The TKE is similar in all grids, indicating the sub-grid scale parameterisations for turbulence are capturing the processes in the lower resolution grids.

3.3. Grid sensitivity summary

The surface current anomalies in Fig. 3 show that as the number of nodes representing the vicinity (150m radius) of the turbine increases by factors of 2.8 and 37.2 (from Fig. 2b to Fig. 2d and Fig. 2f, respectively), the width of the wake decreases from approximately 50m to 30m at 200m from the monopile. Similarly, the structure of the flow around the turbine is less well resolved, although the major characteristics of the flow remain. This distribution matches that seen from Computational Fluid Dynamics (CFD) modelling (e.g. Jensen et al., 2006; Okorie, 2011).

In the vertical transect, the vertical velocity distributions are similar across the three flume grids (Figs. 3b, 3d and 3f), with all three generating the same broad structure in the local vertical velocity field. The main impact resolution has is in resolving unsteady flow in the wake of the monopile which yields vertical velocity structures associated with eddies shed from the monopile. This unsteady flow is absent in the low and medium resolution grids, as is the corresponding downstream detail in the vertical velocity.

Tab. 1 shows that the low and medium resolution flume grids produce similar results, but that when the number of nodes in the vicinity of the turbine increases by a factor of 37, the three integrated parameters show that the monopile impacts in the high resolution grid are greater than in the low and medium resolution grids. Thus, the sub-grid scale horizontal and vertical parameterisations underestimate the impacts arising from the monopile and therefore a lower resolution grid provides a lower bound on the potential impacts.

The grid sensitivity analysis performed here shows that lower resolution grids are able to capture similar structure as more detailed ones, however, that is not the only consideration when investigating impacts across the shelf. Including a realistic number of wind turbine monopiles within a shelf-scale model means that it is computationally unrealistic to include the highest resolution configuration from the flume testing. Since there are 242 wind turbine monopiles in the eastern Irish Sea, describing them with the low resolution configuration here requires 81,554 nodes. The medium and high resolution grids increase that number to 228,206 and 3,038,068, respectively. On top of those numbers is the number of nodes required to describe the rest of the

Grid	Speed anomaly ($m^3\ s^{-1}$)	TKE ($cm^3\ s^{-2}$)	Potential energy anomaly ($J\ m^{-1}$)
Low	1196.8	124353.6	228001.6
Medium	1169.6	132295.5	231875.3
High	784.4	121363.1	182797.6

Table 1: Summary variable values used to assess the flume grid resolution sensitivity (Fig. 3).

model domain, which for a 1-10km resolution domain requires an additional 58,500 nodes. Assuming that increasing the number of CPUs over which the model can run yields a linear decrease in run time, this still represents an unrealistic configuration given the computation resources available at this time.

Based on the results of the grid sensitivity analysis and the requirement to maintain a realistic run time, a shelf scale model with the turbines and the immediate vicinity represented by a configuration similar to the low resolution flume test will be used to describe the 242 wind turbines in the eastern Irish Sea.

4. Shelf model

The use of a traditional regular grid (i.e. rectangular or curvilinear element shapes) to model both individual wind turbine monopiles (5m diameter) as well as shelf-scale circulation within the same grid is impractical due to the extremely large number of elements such a domain would require. Unstructured grids can be created to resolve wind farm monopiles whilst areas outside the wind farms can be represented with a coarser network of elements, minimising the overall number of computational nodes. The grid sensitivity analysis in Section 3 illustrates the impact the resolution has on the predicted hydrodynamics. Based on that analysis, Fig. 1 shows the model domain and the grid configuration within a wind farm in the eastern Irish Sea. In total, the current set of seven wind farms in the eastern Irish Sea, comprising 242 individual turbine monopiles, are included in the model grid. The two grids used in the comparison differ only insofar as the wind turbine monopiles are filled in with six new elements.

4.1. Grid configuration

The model domain is defined by the initial coastline, derived from the Global Self-consistent, Hierarchical, High-resolution Shoreline (GSHHS) (Wessel and Smith, 1996) and sampled at resolutions between 200 and 1200m. The model grid is constructed such that the resolution is controlled by a size function based on coastline curvature, water depth (h), bathymetry gradient and gravity wave propagation speed ($\sqrt{gh}$, where g is the acceleration due to gravity ($9.81 m\ s^{-2}$)) (Fig. 1). This ensures that areas with complex coastlines, high seabed gradients and shallow water depths have smaller elements to ensure tidal wave propagation is well resolved (Legrand et al., 2007). The gradient control is depth-limited (50m threshold) so only the shallowest parts of the domain are adjusted by both the water depth and its gradient (otherwise water depth only). From an initial grid, the unstructured grid is iteratively adjusted such that the element sizes fit the size function. Final manual adjustment of the grid ensures the quality criteria in the FVCOM manual (Chen et al., 2013) are met. The model has 20 vertical layers distributed in the vertical with a quadratic function (the resolution of the surface and near-bed layers is higher than those in the mid-water column).

Due to the large computation requirements associated with running a grid in which each monopile is explicitly described in the grid (grid A), a separate coarser grid (grid B) is used for the tidal analysis. Grid B uses the same coastline and bathymetry data, as well as the same constraints in the size function, but the elements which describe the turbine monopiles are omitted. This yields a grid with approximately 107,000 elements (from 58,500 nodes) which is run for 6 months.

In contrast, grid A contains approximately 295,000 elements constructed from 153,000 nodes; element sizes range in size from 10km at the open boundaries to 2.5m at the wind turbine monopiles (Fig. 1).

4.2. *Shelf model set up*

Circulation within the model is driven by predicted surface elevation from thirteen tidal constituents (M_2, S_2, N_2, K_2, K_1, O_1, P_1, Q_1, MF, MM, M_4, MS_4, MN_4) input at the three open boundaries (comprising 200 nodes, red lines in Fig. 1) calculated at 10 minute intervals from the TPXO Tidal Model Driver (TMD) MATLAB toolbox (Egbert et al., 1994; Egbert and Erofeeva, 2002) using the OSU Tidal Inversion Software (OTIS) European regional tidal solution (Egbert et al., 2010). The temperature and salinity along the open boundaries are nudged with global Hybrid Coordinate Ocean Model (HYCOM) daily data (Bleck and Boudra, 1981; Bleck, 2002) and interpolated in space (horizontally and vertically) to the open boundary nodes. The HYCOM model data are also used to initialise the model vertically resolved temperature and salinity fields (i.e. initial conditions include stratification in May). The model is spun up for two days to allow the velocity and turbulence fields to stabilise.

River discharge rates were obtained from the European Hydrological Predictions for the Environment (E-HYPE) model output (Donnelly et al., 2012) for 173 rivers in the model (black dots in Fig. 1a). River salinity and temperature data are not provided in the E-HYPE model output and continuous sampling of the rivers in the area is sporadic. River nodes in the model grid are located within regions of tidal influence and therefore non-zero salinities were used to account for estuarine mixing. Salinities were set to one of five constant values (25, 27.25, 29.5, 31.75 and 34) depending on the distance from the E-HYPE river positions (fresher for a small distance and vice versa). Historic temperature data from the UK Environment Agency's Freshwater River Temperature Archive (Orr et al., 2010) was used to generate temperature climatologies for the 30,000 records in the archive. For each river input, the closest river temperature climatology was used; river nodes outside the coverage of the temperature climatology use the mean of the 30 closest climatologies.

The effect from surface heating within the model is included from the National Centers for Environmental Prediction and Department of Energy Atmospheric Model Intercomparison Project (NCEP-DOE AMIP-II) Reanalysis-2 heat flux data (Kanamitsu et al., 2002) interpolated to the model grid. Heat flux is prescribed at the surface and added to the water column using the COARE2.6 bulk air-sea flux algorithm (Fairall et al., 2003) in the vertical diffusion terms as layer fluxes. Precipitation and evaporation are included from the higher spatial and temporal resolution UK Met Office Unified Model (MetUM) output. Although the wind turbine superstructure induces additional atmospheric turbulence (Hasager et al., 2013), the magnitude of the effect at the sea surface is limited compared with that at the rotor height (Christiansen and Hasager, 2005). Furthermore, the impact induced in the water column from this altered surface stress is of the order $0.04\,\mathrm{mm\,s^{-1}}$ in the vertical and $0.1\,\mathrm{m\,s^{-1}}$ in the horizontal (Ludewig, 2015). Although the reduction in horizontal current speeds represents approximately 5-10% of the maximum tidal speeds in the region, we omit wind forcing from the model to focus on the impacts generated by the physical presence of the turbine monopiles only.

Water depth within the model domain is derived from the Proudman Oceanographic Laboratory Coastal Ocean Modelling System (POLCOMS) High Resolution Continental Shelf (HRCS) grid (2km horizontal resolution) for the majority of the domain whilst the vicinity of the wind turbines is from bathymetry from the Liverpool Bay Coastal Observatory (CObs) (10m horizontal resolution). Water depth for each grid node is calculated by linearly interpolating the scatter data. The bed roughness length (z_0) is uniform within the domain (0.03m).

The model is run for two periods: January and May. The north-west European continental shelf is season-

ally stratified, with stratification typically beginning in April. By modelling January and May, we are able to include both fully mixed and stratified waters to investigate how the turbines affect stratification.

5. Model validation

5.1. Tidal harmonics

The computational expense of running the model grid with the wind turbine monopiles included means a sufficiently long time series for a comprehensive harmonic analysis (including long period constituents) is impractical. To ensure the modelled surface elevation in FVCOM accurately reproduces the major tidal constituents, a simplified grid (grid B) without the turbines was generated and run for 6 months. These results were analysed using UTide (Codiga, 2011) in MATLAB to calculate the major constituent amplitude and phases. Despite the relatively minor contribution from the overtides (e.g. M_4) to the tidal energy, their spatial distribution and magnitude serve as an important test of whether the principal harmonics have been accurately reproduced (Jones et al., 2009). Given the sensitivity of modelled tides to the domain size and shape (Davies and Jones, 1996; Zhou et al., 2014) and since the introduction of wind turbine monopiles changes these factors, it is important that these higher harmonics are investigated. Fig. 4 shows amplitude and phase of the M_2, S_2 and M_4 tidal constituents for the model domain. The M_2 and S_2 tidal constituents account for in excess of 95% of the tidal signal within the model domain and M_4 is important in shallow coastal regions and the propagation of the tidal wave from the model boundaries across the shelf domain (Jones and Davies, 2007a).

The amplitudes and phases for M_2, S_2 and M_4 in Fig. 4 show a high similarity with existing model analysis (e.g. Jones and Davies, 2007a,b; Jones et al., 2009), with observation derived maps (Proudman and Doodson, 1924; Doodson and Corkan, 1933) as well as with remote sensing analyses (Egbert et al., 1994; Andersen, 1995). The major features of the UK shelf tidal system have been captured, including the placement of the amphidromes (including the degenerate amphidromes) and areas of large tidal ranges. The agreement in the coastal distribution of the M_4 tide and the existing analyses indicate that the model bathymetry is sufficiently accurate to allow the M_2 tidal wave to propagate and interact with itself (the process by which the M_4 overtide is generated).

To compare the modelled surface elevations with those from observations, the BODC repository of coastal surface elevation time series (the National Tidal and Sea Level Facility (NTSLF) tide gauge records) and the historic bottom pressure sensor time series were downloaded. In total, 95 coastal and offshore locations were available for analysis. These data provide a good spatial coverage across the domain (Fig. 1a). Comparisons of the coarse grid modelled surface elevation with the BODC time series are shown in Fig. 5 for the M_2, S_2 and M_4 constituents. In aggregate, amplitude and phase Root Mean Square Error (RMSE) values for the three components are 11.9cm and 4.7°, 5.1cm and 6.8° and 2.5cm and 21.5° for M_2, S_2 and M_4, respectively. The M_4 amplitudes are slightly over-predicted relative to the observations suggesting that the M_2 tide is correspondingly too high, though the magnitude of the difference is small. Those sites with larger differences (shown as the cluster of points which lie above the 1:1 ratio line in Fig. 5a) are mainly located in the Severn Estuary, a part of the model domain with the largest tidal range, and therefore one in which small differences in the predicted tidal elevation cascade down to the overtides resulting in correspondingly large amplitudes in Fig. 5e.

For modelling the impacts of wind turbines, the grid A configurations (with and without individual monopiles) are significantly more detailed and thus require more computational run time. To ensure the model results from the shorter grid A results are comparable to the longer grid B run, Fig. 6 shows the surface elevation from three locations within the model domain from the grid B (coarse), and grid A (fine, with and without turbines) grids. The differences between the two grid A model runs (with and without turbines) are imperceptible

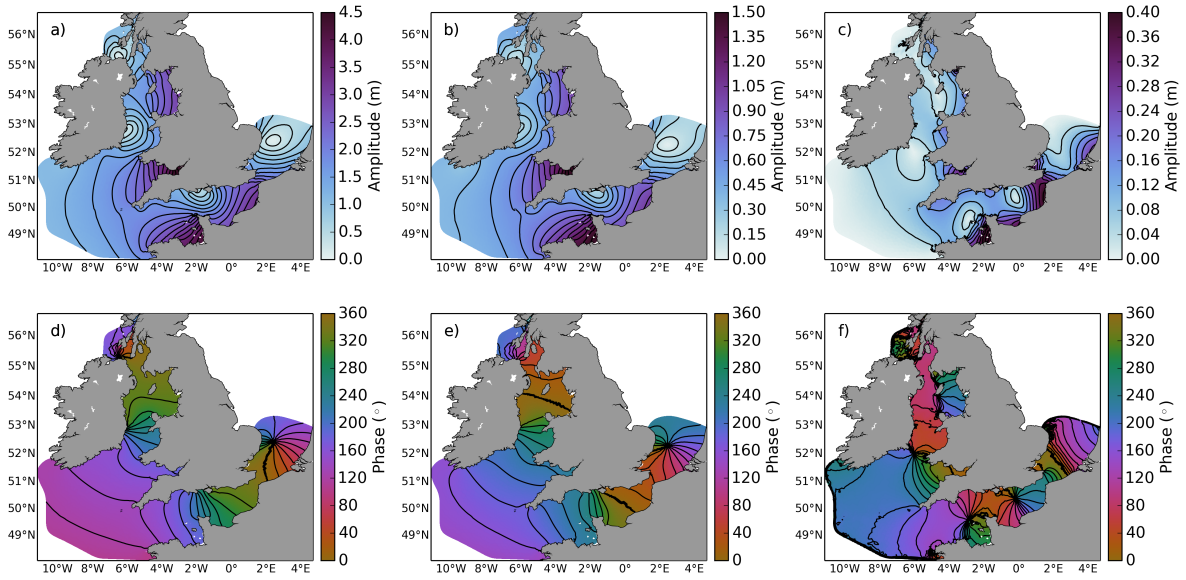

Figure 4: M_2, S_2 and M_4 amplitude (a–c) and phase (d–f) from the coarse grid.

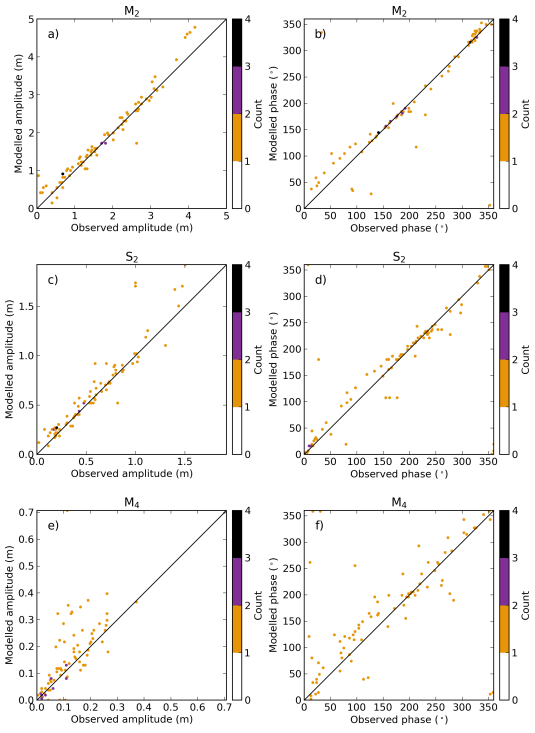

Figure 5: M_2, S_2 and M_4 amplitude (a, c, e) and phases (b, d, f), respectively, from the model against the values from 95 observed time series. Colours indicate the number of samples at the given bin size (100 bins in x and y).

ble. Between the grid A and B results, the differences are small and can be accounted for by the inclusion of wind and air pressure surface forcing in the grid B run compared with the grid A run. The comparison between the different grid A set ups (with and without turbines) indicates they reproduce the same tidal structure as in grid B.

5.2. *Fine-scale coastal circulation*

The fine grid modelled surface velocities were compared with high frequency radar data to assess spatial model skill at reproducing coastal currents. The Liverpool Bay Coastal Observatory (CObs) provides 20 minute resolution time series of 4km spaced surface velocity vectors over 4,700km^2 from August 2005 to December 2011 (Howarth et al., 2007), whilst a second radar installation along the north Cornish coast (from the Partnership for Research in Marine Renewable Energy (PRIMaRE) project) provides hourly 2km spatial resolution surface velocity vectors over 1,800km^2 for 2011.

In the analyses which follow, for each radar grid point, the nearest model grid A point is found and its time series used in the comparison. Since the model

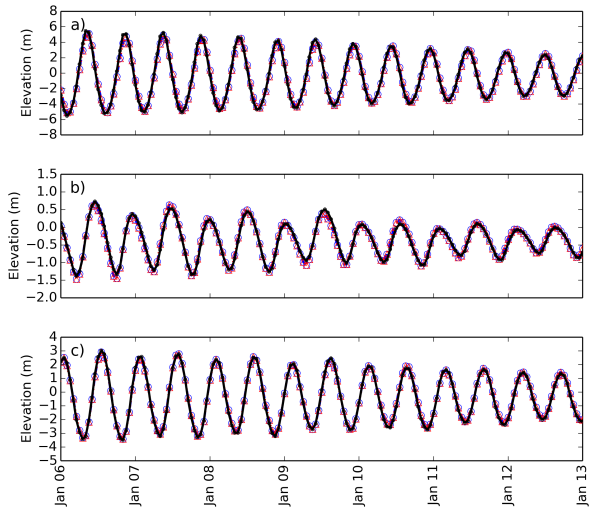

Figure 6: Comparison of the modelled surface elevation for January 2011 from the long time series coarse grid (black line with dots) and the two short time series fine grids (with and without turbines, blue dashed line with open circles and red dotted line with open triangles, respectively) for the a) Severn Estuary, b) central Irish Sea and c) eastern Irish Sea.

grid is usually higher resolution (the model grid resolution varies so this is not always the case), this approach means no interpolation effects are introduced into the comparisons. The radar data are preprocessed to eliminate gaps in the time series and subsequently interpolated to the coarser model output time series. This process ensures each data set has the same number of data points to allow the calculation of the bias, correlation and RMSE. The maximum value in the observed time series at each grid point is used as the upper bound against which the statistics are compared.

5.2.1. *Liverpool Bay Coastal Observatory radar*

The time series analysis of the data from Liverpool Bay CObs yields a correlation over the majority of the domain in excess of 0.8 (Fig. 7a). In areas where the number of samples (Fig. 7b) is lower (i.e. close to the radar sources), the coefficient decreases. This, however, does not explain the entirety of the difference: the lower correlation occurs mainly along the south-eastern edge of the coverage and is matched by a bias of $\sim -5\%$ (i.e. the model under-predicts by 5%) and RMSE values of up to 15% of each grid's maximum in time (limited to the model duration). To better grasp the potential causes of these differences, Fig. 8 shows a time series of surface current speed at two locations: one along the south-eastern boundary of the coverage and the other within the region of higher correlation (locations A and B in Fig. 7, respectively).

The radar time series from site A (poor correlation) contains a large number of spikes up to double the modelled values, whilst site B (high correlation), has no such spikes. Thus, the reason for the poor correlation is noise in the radar data. The time series at location B has an RMSE of 10.7% of the maximum (in time), despite the lack of wind in the model calculation. The proximity of these regions of poorer correlation does partially overlap the locations of the wind farms, where the turbines can interfere with the radar (Robinson and Wyatt, 2011; Robinson et al., 2013), but not consistently and is therefore unlikely to be the cause of the discrepancies. The discrepancy of $\sim 0.2\,\mathrm{m\,s^{-1}}$ around 8th January in Fig. 8 is instead likely the result of the increased wind speeds which are not included in the model set up (supported by the increased noise in the results at location A and the Hilbre Island wind gauge data in Fig. 8); similarly, the over-predicted modelled speeds on the 11th and 12th January may be due to wind driven surface circulation opposing the tidal circulation. Overall, the model reproduces the asymmetry in the surface current speeds and the spring-neap cycle.

5.2.2. *PRIMaRE radar*

The model-PRIMaRE radar statistical analysis results are shown in Fig. 9. Compared with the CObs data, the PRIMaRE data are noisier with artefacts from the radar visible in the statistical analyses (the large arcs in Fig. 9a). Although the spatial resolution is higher here than in the CObs data, the time sampling is hourly compared with every 20 minutes. The correlation coefficient in Fig. 9a gives a median value across the domain of 0.72. In contrast with the CObs data, where the correlation improved with distance from the radar sources, the correlation decreases with distance and sampling density (Fig. 9b): when the number of samples falls below 300,

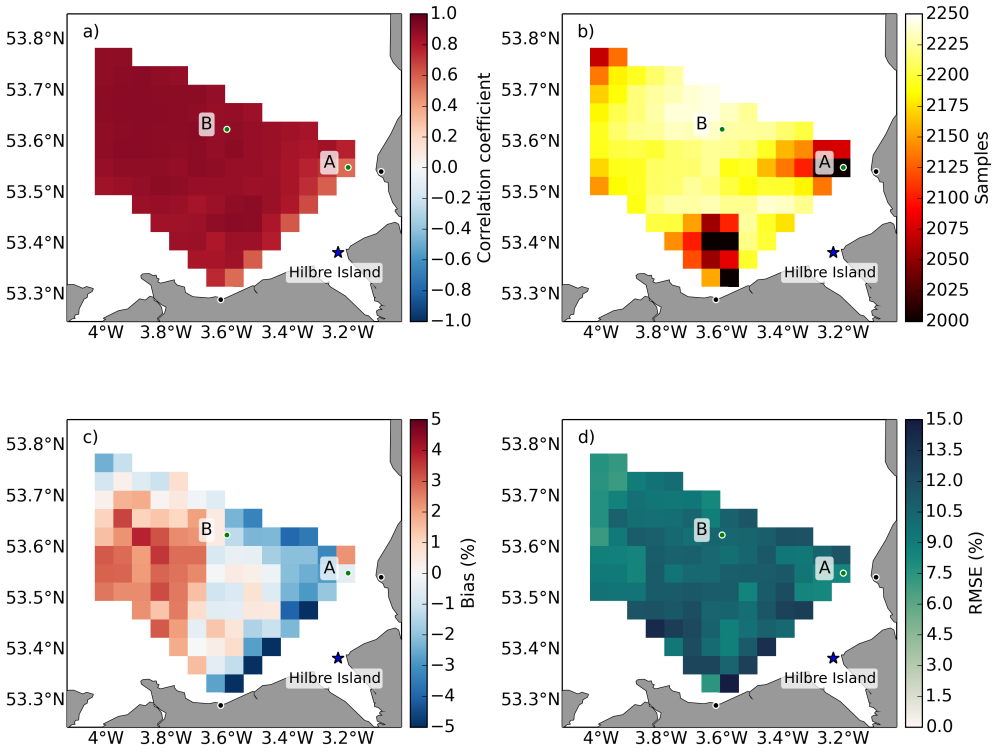

Figure 7: Time series analysis of the CObs radar surface velocities and the corresponding modelled velocities. Panels a–d show the correlation coefficient where $p < 0.05$, number of samples from the CObs data, bias (as a percentage of the maximum at each location) and RMSE (as a percentage of the maximum) between the radar and modelled data, respectively. Locations with fewer than 500 samples are omitted from the analysis. Black dots indicate the locations of the two radar sources. Green dots (marked A and B) indicate the locations of the time series in Fig. 8. The blue star indicates the location of the CObs Hilbre Island wind gauge.

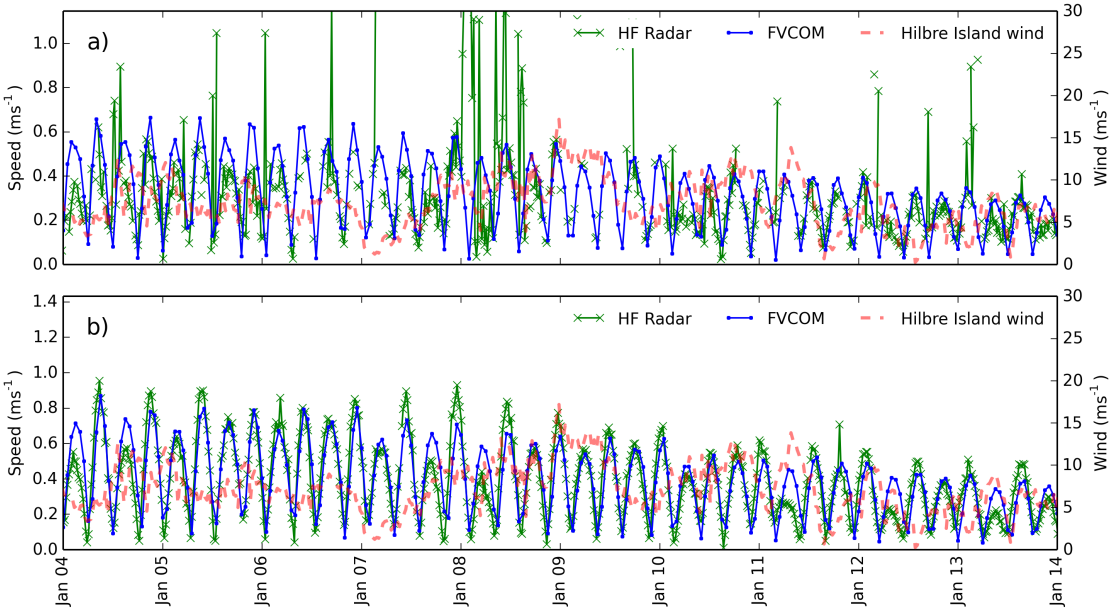

Figure 8: Time series of the surface speed at two locations within the CObs data (see Fig. 7) illustrate the poorer match between model and observation. Panel a) shows the time series within the poor correlation (location A) region and panel b) within the high correlation region (location B). Dotted red lines indicate wind speed measured at Hilbre Island (8km from the south-eastern boundary of the radar coverage).

the correlation dips below 0.5.

Fig. 9c shows the results of the bias between the modelled and observed surface velocities. The model over-predicts surface currents close to the coast by 2% of the maximum values. Further offshore, however, the modelled surface currents are under-predicted by 1% of the maximum at each grid point. This discrepancy is due to the relatively coarse grid in this area (approximately 2.5km) since the model grid A resolution decreases with distance from the coast (see Section 4.1). Nevertheless, surface velocities are typically within 10% of the observed values across the majority of the domain.

5.3. Validation summary

Tidal analysis of the model results against a range of observed data, including HF radar data and coastal and offshore tide gauges, has shown the model accurately reproduces the physical environment of the model domain. The ranges in Bartlett (1998) for numerical model performance in coastal and estuarine areas are well satisfied for both the spatially varying and point time series results: modelled coastal and offshore tide amplitude and phases differ from observations by 10% (within the recommended 15% range) and 5-10% for currents (recommended 10–20%) at both HF radar locations (CObs and PRIMaRE).

6. Results

The anticipated impacts from the introduction of a large number of monopiles into an energetic shelf sea are that locally generated increased turbulence dissipates rapidly and the impacts are limited to the near-field. These local impacts would be evident in the velocity fields, mainly as reductions in the wakes, but also increases around the monopile sides. Since the shelf sea is a large dynamic system, alterations in the energy balance at OWF-scale would be accommodated by altering the flows within a relatively short distance (a few tens of kilometres) and beyond that, little to no impact would be evident in the circulation.

In the vertical structure of the water column, the local effects would be relatively marked, with potentially increased mixing due to turbulence from the monopiles. This would be evident only in areas which experience seasonal stratification and in which the maximum current speed is high enough to create turbulent fields able to induce vertical mixing. Beyond the OWFs, the impact is likely to be relatively minor.

Analysis of the spatial and temporal changes in the modelled hydrodynamics can identify how the introduction of the monopiles alters the circulation in both the near- and far-fields. An initial qualitative analysis of the surface current speed is used for comparison of the wake size and shape in the remote sensing surface roughness (Li et al., 2014) and Suspended Particulate Matter (SPM) concentration (Vanhellemont and Ruddick, 2014). Far-field effects are analysed through tidal elevation harmonic analysis to extract the major semi-diurnal tidal constituent (M_2) to compare the spatial distribution of amplitude and phase between the two model outputs (with and without turbines). The impacts on circulation from the monopiles are characterised in the horizontal through analysis of the velocity field and in the vertical through the water column structure and the potential energy anomaly (a measure of the water column stratification).

6.1. Surface wake characteristics

Figure 10 shows four snapshots of the surface speed anomaly (the instantaneous surface speed subtracted from the monthly mean surface speed). Although the remotely sensed wind farms are in different parts of the world (southern North Sea for Vanhellemont and Ruddick (2014) and East China Sea for Li et al. (2014)), they have similar wind farm configurations, with turbines organised in rows of 10–15 turbines spaced approximately 1km apart and each row separated from its neighbour by 2–3km. The OWF in Fig. 10 (“Ormonde”) has turbines spaced 400m apart and the rows 1.2km apart.

The wakes observed from remotely sensed imagery (Li et al., 2014; Vanhellemont and Ruddick, 2014) indicate they extend up to 1.3km from the wind turbine

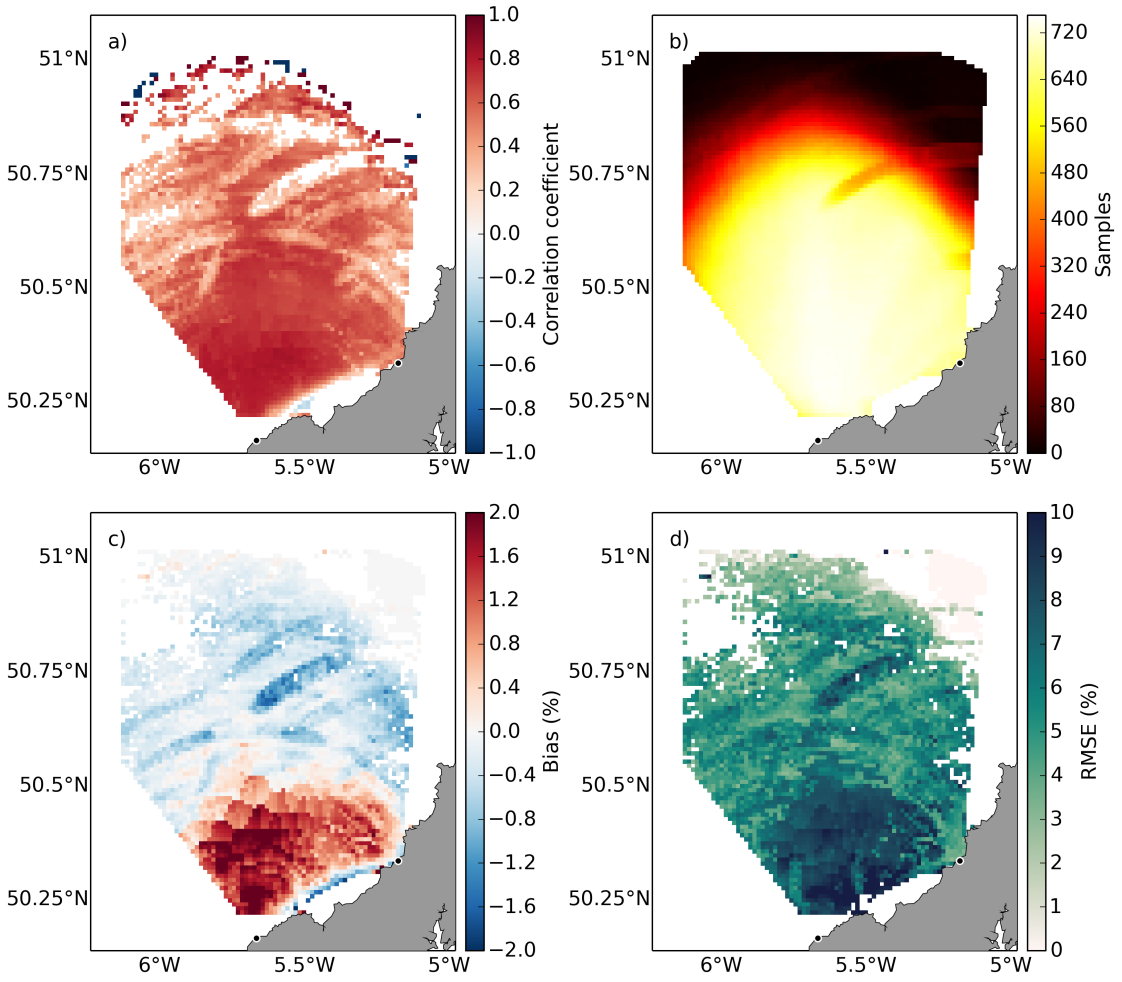

Figure 9: Time series analysis of the PRIMaRE radar surface velocities and the corresponding modelled velocities. Panels a–d show the correlation coefficient where $p < 0.05$, number of samples from the CObs data, bias (as a percentage of the maximum at each location) and RMSE (as a percentage of the maximum) between the radar and modelled data, respectively. Locations where the speed accuracy is less than $0.3\,\mathrm{m\,s^{-1}}$ are omitted from the analysis. Black dots indicate the locations of the two radar sources.

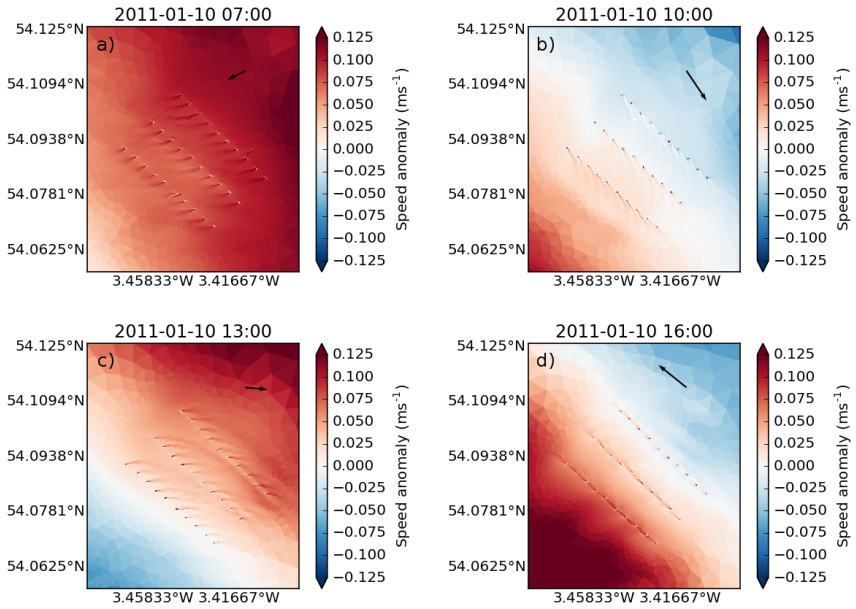

Figure 10: Snapshots of surface current speed anomaly at three hourly intervals during a spring tide, highlighting the spatial and temporal evolution of wakes surrounding the monopiles. Black vectors show the background surface current conditions at a location outside the influence of the OWF (vector maximum speed is 0.34m s^{-1}).

and are 100–150m wide, independent of current direction; modelled wakes from Fig. 10 are similarly scaled with maximum lengths of 1.1km and widths of 100m. The modelled temporal evolution of the wakes indicates their orientations align with the surface current direction, although their length remains independent of the current speed. As the tide turns (Fig. 10b and c), the wakes are curved and individual wakes merge into areas of consistent change in surface current speed relative to the background values. When the tide flows parallel to the turbines (Fig. 10d), the wakes are completely merged into a single structure extending from one end of the OWF to the other.

For the size of the turbines in the model grid (5m diameter), the wakes are up to 250 times the monopile diameter, a factor which is ten times higher than that found from existing 2D wind farm modelling in the western Irish Sea (MRG Consulting Engineers Limited, 2013) for similar speed reductions (5cm s^{-1}). Both regions have tidal regimes with maximum current speeds of 1m s^{-1} and similar wind farm configurations (500m turbine spacing with rows 1.5km apart). The only major domain difference is the water depth in which the turbines are placed, with the Dublin Array set in 10m of water compared with the majority of the wind farms in the eastern Irish Sea in waters between 20 and 30m deep. Thus, it appears the inclusion of the vertical dimension in the modelling performed here increases the sensitivity of the hydrodynamics compared with the 2D depth-averaged modelling performed for the Dublin Array.

6.2. *Tidal harmonic distribution*

Fig. 11 shows the percentage difference in the amplitude (a) and phase (b) of the M_2 tidal constituent between the two grid A model results (with and without turbines) relative to the M_2 amplitude from grid B (for those magnitudes, see the results from the long term grid B model run in Figure 4a). The majority of the domain sees an increase in the tidal amplitude whilst the phase is less affected; almost the entire Celtic and Irish Sea regions see changes of less than 0.2° in phase compared with almost no parts of the domain experiencing changes of less than 0.2m in amplitude. There are no

changes along the open boundaries since the model is forced with the same tidal elevation time series for each grid.

The amplitude in Morecombe Bay (MB in Fig. 11) increases by a maximum of 7% with the introduction of the turbines. Increases of 1–2% occur in the Solway Firth (SF), Isle of Wight (IOW), Severn Estuary (SE), Thames Estuary (TE) and at Antwerp (AW). The Gulf of St Malo (GSM) shows almost no change in amplitude (less than 0.4%) which, given the 4m M_2 amplitude (Fig. 4a), represents a change of less than a 2cm.

The harmonic analysis in Fig. 4 identifies the four M_2 amphidromes within the model domain, moving anticlockwise around England: in the North Channel of the Irish Sea; along the east coast of Ireland; along the southern English coast; in the southern North Sea. The second and third of those are degenerate amphidromes whilst the first and last are offshore. Comparing the areas of largest change with the overall distribution of the M_2 amplitude in Figure 4a shows that they occur in macrotidal areas and close to the amphidromes. The majority of the change in amplitude and phase in Fig. 11 can be seen in the vicinity of these amphidromes, where a small change in the amphidrome location results in a large percentage change in amplitude and phase. However, the sensitivity of the location of the amphidromes is closely linked with their proximity to the open boundaries, thus changes in their locations may reflect model limitations (Zhou et al., 2014) rather than changes in the hydrodynamics within the model due to the introduction of the turbines.

The two offshore amphidromes (North Channel of the Irish Sea and in the southern North Sea) exhibit the largest changes. Analysis of their grid locations shows that the southern North Sea amphidrome has shifted north-east by 4.3km with the introduction of the turbines, whilst the North Channel amphidrome remains in the same location. The large amplitude and phase difference in the latter is instead a change in distribution around the amphidrome rather than a shift in its position following the introduction of the turbine monopiles.

6.3. Vertical water column structure

The turbine monopile impacts on the vertical structure of the water column are illustrated in vertical profiles through six wind turbines in Fig. 12. Four parameters are shown: horizontal current speed (a), vertical velocity (b), temperature (c) and salinity (d).

With the tide flowing from left to right in Fig. 12a, the lee of each monopile has a decreased velocity extending 200m downstream, with the impact decreasing with distance from the monopile. Vertically, the horizontal velocity impacts are largest in the upper water column, with differences between the unaffected regions and at the monopiles of 0.3–0.5m s^{-1}. The pattern of vertical velocity in Fig. 12b shows reversed flow either side of the turbine, with downward vertical flow upstream and upward flow downstream. Magnitudes of the vertical flow are $\pm$0.1m s^{-1} but over a limited extent (within 20m of the monopile) before returning to zero over the majority of the transect. The vertical velocity magnitudes are controlled by distance from the surface and seabed boundary layers (vertical velocities in those layers are necessarily zero) and the magnitude of stratification. Stratified water will experience smaller vertical velocities than their fully mixed counterparts due to the increased work required to overcome the density gradient.

As the water column stratifies due to increased surface heat in the spring, the impact of the monopiles is evident (Fig. 12c and 12d). The downward motion of water upstream of the turbine entrains warm, fresher surface water into the cooler, more saline subsurface layer, whilst the upward flow downstream of the turbines pushes cooler water into the surface layer. Figs. 12c and 12d show this exchange occurs in the top 10m of the water column, where the stratified layer is approximately 5m thick. As the tide turns and water flows around different parts of the monopiles, a radius of approximately 200m develops around each monopile over which increased exchange occurs.

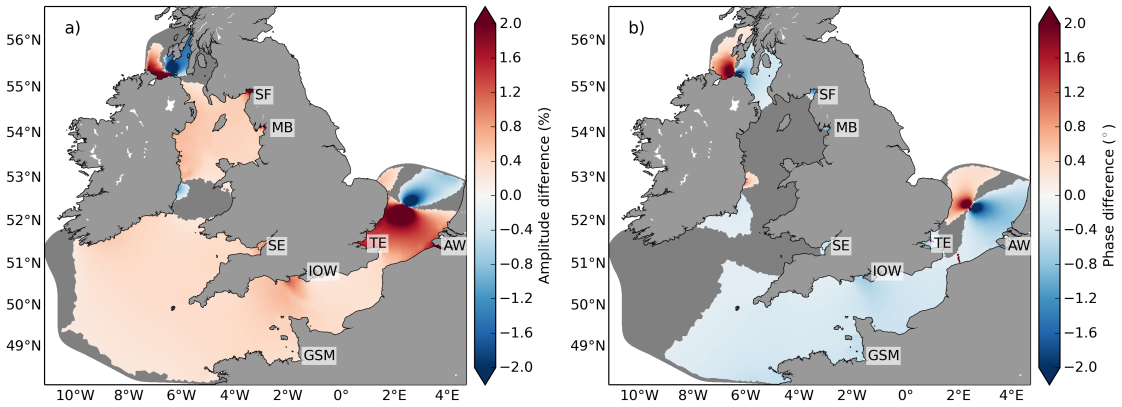

Figure 11: Difference in M_2 amplitude and phase between each model grid output. The amplitude difference is expressed as a percentage of the amplitude for the without turbines model run. Negative change indicates a decrease in amplitude with the introduction of the turbine monopiles and vice versa. SF = Solway Firth, MB = Morecombe Bay, SE = Severn Estuary, GSM = Gulf of St Malo, IOW = Isle of Wight, TE = Thames Estuary, AW = Antwerp. Grey indicates a change of less than 0.2% in amplitude or 0.2° in phase.

6.4. Seasonal stratification

In seasonally stratified seas (such as those around the UK), the stratification can be measured through the potential energy anomaly. The potential energy anomaly represents the amount of energy required to fully mix the water column, thus, a value greater than zero indicates a stratified water column, less than zero means the column is convectively unstable (i.e. less dense water below high density) and zero a fully mixed water column. The climatic conditions of the north-west European continental shelf mean that the water column stratification onset is controlled by decreased wind stress and freshwater inputs and increased summer insolation creating a warm and slightly more saline surface layer which is able to persist despite strong tidal mixing, inducing a stratification feedback (Holt and Umlauf, 2008). Tidal mixing during the winter is able to overcome these stratifying factors to produce a fully mixed water column.

Fig. 13 shows the mean modelled potential energy anomalies in the eastern Irish Sea in early May 2011 with (a) and without (b) the wind turbines; the difference in anomaly between the two model configurations is shown in Fig. 13c. Contours overlain are the theoretical front positions predicted by the Simpson-Hunter parameter $S = log_{10}(h/u^3)$. The stratification from the model extends along the centre of the bay, matching both the Simpson-Hunter position as well as results from existing modelling and observations (Holt and Umlauf, 2008).

The majority of the wind farm turbines in the eastern Irish Sea lie in the relatively shallow (approximately 20m depth) well mixed waters, particularly close to Liverpool Bay and the north Welsh coast. The major difference in stratification is confined to the largest wind farm which, coincidentally, straddles the tidal mixing front. The inclusion of the wind turbine monopiles has affected the stratification up to $\pm 0.5\,\mathrm{J\,m^{-3}}$, or 5–15% of the anomaly in Fig. 13a, mainly as a decrease, over an area of approximately $250\mathrm{km}^2$. The closest wind turbines in the four wind farms adjacent to the potential energy anomaly impact region (Fig. 13c) contain 162 monopiles with a footprint of $3{,}180\mathrm{m}^2$. Thus, the spatial extent on the stratification is a factor of approximately 80,000 times their combined horizontal area.

Figure 14 shows the evolution of the potential energy anomaly in the eastern Irish Sea for early May 2011. The strength of stratification is dependent on the tide, with maximum stratification occurring as the tidal speed decreases. Stratification continues to increase as the surface insolation increases. As each successive tide increases in speed, the stirring effect from the wind

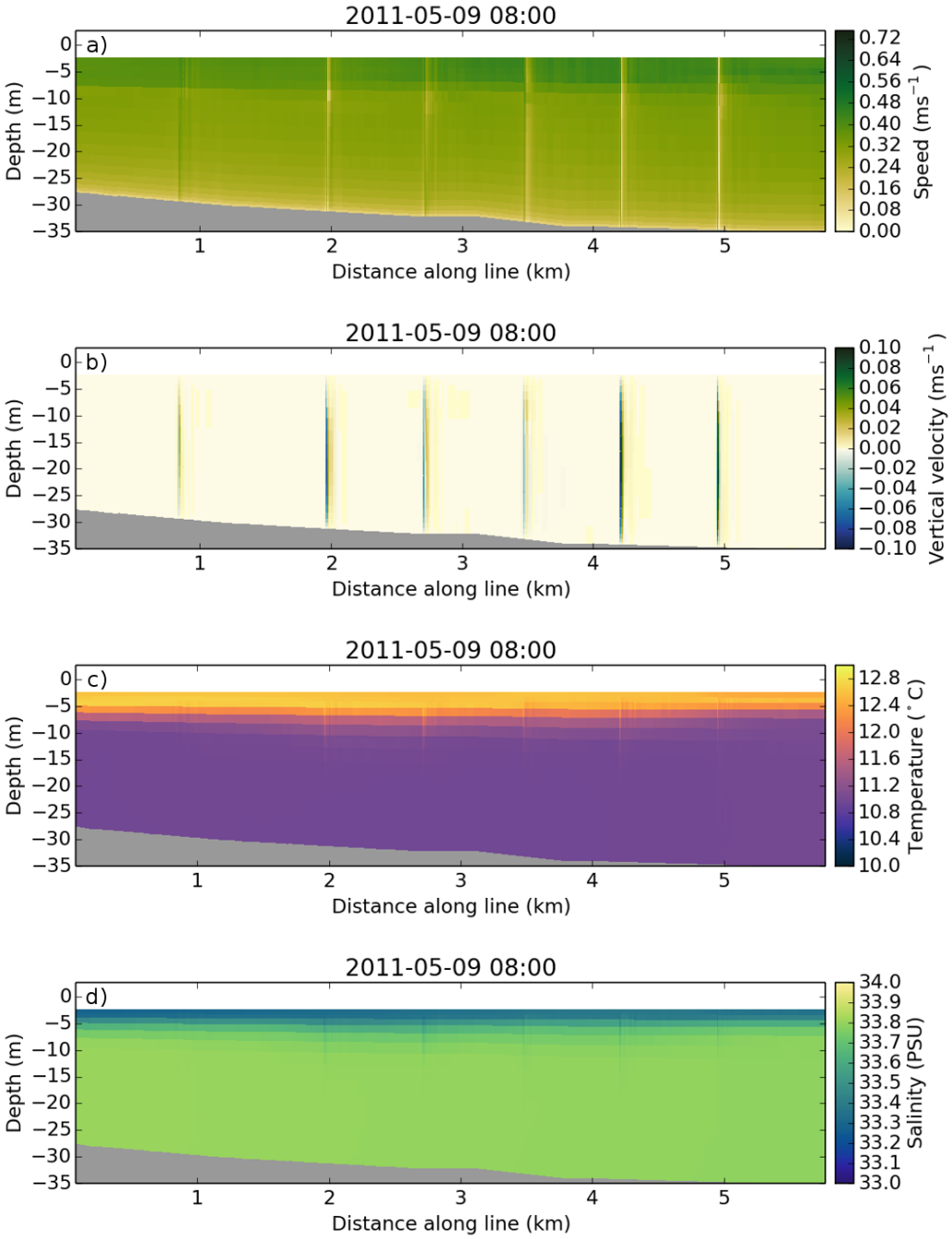

Figure 12: Transect through six wind turbine monopiles showing water horizontal speed (a), vertical velocity (b), temperature (c) and salinity (d).

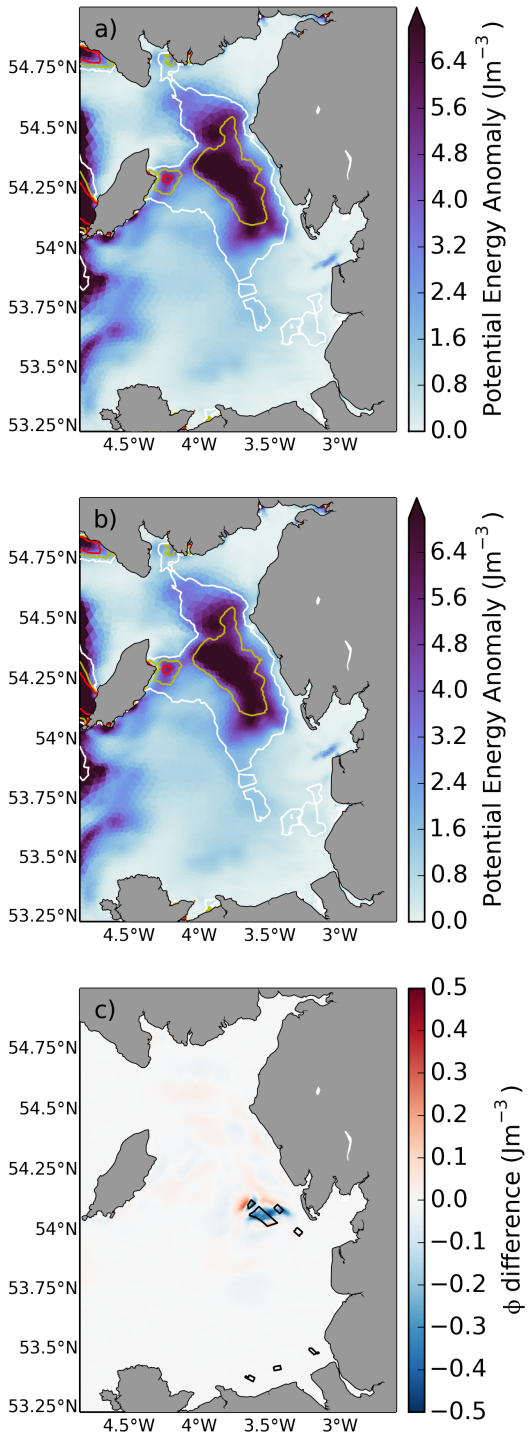

Figure 13: Potential energy anomaly plots from May 2011 for the no turbine (a) and turbine (b) grids. The difference between the two anomalies is shown in c. Black polygons in c) indicate the OWFs. Contours in a) and b) show the Simpson-Hunter parameter with values of 2.0, 2.4 and 2.8 (white, yellow and red, respectively) as an indicator of the theoretical location of fronts (Simpson and Hunter, 1974; Bowers and Simpson, 1987; Holt and Umlauf, 2008).

turbine monopiles increases, decreasing the stratification relative to the results from the grid without turbines. The inclusion of the wind turbine monopiles has decreased stratification at this location, although Fig. 13 shows both increased and decreased stratification around the wind farms.

7. Discussion

The modelling presented here quantifies how the introduction of 242 offshore wind turbines impacts a tidally dominated, seasonally stratified shelf sea. The turbines are explicitly represented in the model grid rather than parameterised through roughness or momentum effects (Melville and Sutherland, 1989; Yang et al., 2013). The model is compared against a range of in situ observations (NTSLF tide gauges, BODC offshore pressure sensors, CObs and PRIMaRE HF radar) both as 1D and 2D time series and through harmonic analysis. The results of the model validation indicate that the model performs well within the expectations required for accurate coastal and estuarine modelling put forward in Bartlett (1998).

The approaches taken to quantify the impacts of OWFs so far have had some important limitations, including: turbine representation through grid scaling for computational efficiency yielding uncertainty in the magnitude of any impacts; nesting with one-way communication only, omitting the potential to generate far-field effects; and sub-grid scale parameterisations which may omit important processes. Nearly all of the existing modelling has concentrated on smaller domains in which the focus of the impacts lies in the region immediately surrounding the wind farm.

Work in which far-field effects on tidal harmonics are looked at from the perspective of sea level rise has shown that relatively small changes in geometry can have impacts at much larger spatial scales. For example, two different approaches to modelling sea level rise (inundation models where rising sea levels flood the land surface in Pelling et al. (2013) compared with

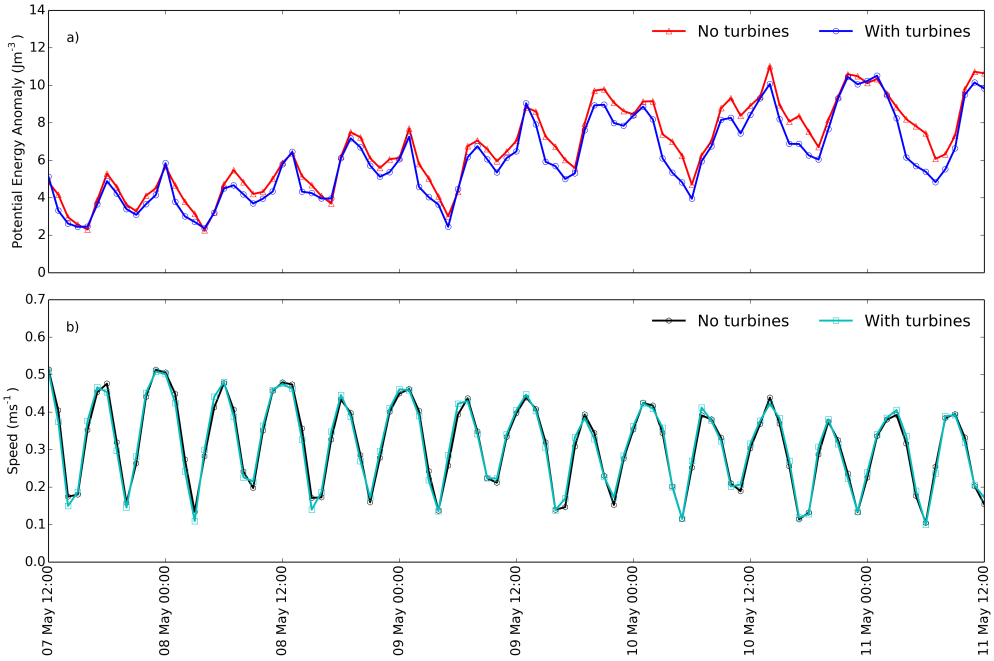

Figure 14: Potential energy anomaly (a) and current speed (b) time series from the eastern Irish Sea (location shown as a star in Fig. 1) for the no turbine and turbine grids.

similar models which use the current coastlines as infinitely high walls in Pickering et al. (2012)) have shown that both the modelling approach and the magnitude of the change in geometry have important roles in how the modelled hydrodynamics are distributed. The introduction of the wind turbines in this model domain has generated similar changes in the hydrodynamics as in Pelling et al. (2013), with shifts in the amphidromes in response to altered basin geometry. Such changes have important consequences for coastal flooding, as the tidal range along the coastline is heavily dependent on the location of the amphidromes, and changes in their position can alter the location and timing of high tides, increasing the likelihood of coastal flooding (Pelling et al., 2013).

The grid sensitivity analysis provides a mechanism to test that the hydrostatic assumptions within FVCOM do not unduly affect the predicted horizontal and vertical structures. At the three flume grid resolutions, the results indicate that a higher grid resolution generates larger impacts from the introduction of a wind turbine monopile. The mechanism by which this takes place is likely to be that impacts from sub-grid scale phenomena are underestimated in the lower resolution grid whilst the higher resolution grids can explicitly represent them, thereby increasing the magnitudes and overall impact at higher resolutions. This means that the shelf scale grid implementation is likely to be a lower bound on the wind turbine monopile induced shelf sea impacts (the magnitudes are generally underestimated with lower resolution). The diagnostic variable magnitudes from the low and high resolution grid sensitivity tests indicate that the impacts from the shelf model configuration used here are between 65% and 80% of the values which might be expected were it possible to model the turbines with the high resolution configuration.

Analysis of the spatial characteristics of wakes expressed in the surface current speed has shown good agreement with the existing remote sensing outputs. Since the modelled wakes generated in the lee of the monopiles remain at all states of the tide, each tidal

turbine has a radius over which its impact is felt. For the turbines in the modelling performed here, the radius for each turbine is approximately 1km, inside of which the reduction in speed is 5% of the regional maximum current speed. Therefore, the spacing of wind turbines within a wind farm has consequences on the total horizontal area which is affected by their introduction. Farms which are more closely spaced therefore minimise the cumulative extent. Previous modelling on wave propagation within model domains indicates that more widely spaced turbines minimise impacts on significant wave heights (van der Molen et al., 2014). Thus, there are opposing factors controlling the distribution of wind turbines within an array which must be reconciled to minimise impacts.

The impact of the introduction of wind turbine monopiles on the M_2 amplitude and phase distribution is significant: over the majority of the model domain, the amplitude has increased by approximately 0.5% whilst specific coastal areas experience changes of up to 7% (e.g. Morecombe Bay). The largest changes (as a percentage of present day amplitude) are seen closest to the amphidromes, however, given the amphidromes represent areas with low amplitudes, such a result is not surprising. In addition, the proximity of the amphidromes with the largest changes to the model open boundaries means the results must be treated with caution there. More important are the changes in coastal environments close to the amphidromes (e.g. the east English coast) and areas which experience increases in excess of 1% (the Solway Firth, Morecombe bay, off the Isle of Wight). Any change in the tidal amplitude in these areas might impact coastal habitats (e.g. intertidal bird nesting grounds) and increase the likelihood of coastal flooding. Given the low lying nature of the east of England, its susceptibility to flooding and its large intertidal area, this is an important future consideration for new OWFs in the North Sea.

In terms of the local changes in hydrodynamics, the monopiles are shown to increase vertical mixing. The mechanism by which this is achieved is a vertical flow along the boundary of the monopile, inducing downward water movement on the upstream side of the monopile and upward flow on the downstream side. In parts of the domain subject to seasonal stratification, this increases mixing in the water column and decreases stratification. Despite the limited horizontal extent of these flows at the monopiles (less than 20m) their impact is felt much more widely, with changes covering approximately 250km^2.

Since monopile obstructions to the flow induce vertical and horizontal mixing in the water column, the introduction of the wind turbines necessarily impacts on the formation of the stratified region (itself dependent on the tidal flow and surface heating (Holt and Umlauf, 2008)). To the south of the eastern Irish Sea, where the water column is fully mixed, the wind turbine monopiles have no measurable impact on the stratification since there is none in the first place. In areas where stratification develops during the year, the wind turbines have changed the hydrodynamics sufficiently to decrease stratification by 5–15%. Holt et al. (2012) calculated changes in the potential energy anomaly and dissolved inorganic nitrogen (DIN) under potential future atmospheric conditions. In the Irish Sea, Holt et al. (2012) find similar changes in the potential energy anomaly for the period between April-June as found here in Fig. 13c (5–15%). The ecosystem modelling in Holt et al. (2012) indicates that there is a corresponding increase in DIN of 5–25%. Thus, the impact of changes in the stratification, when propagated to the ecosystem, can be magnified.

Given the relatively modest size of these OWFs relative to the proposed OWFs in the region, the spatial extent of the impact in stratified waters is significant. Therefore, should future OWFs be placed in stratified waters or along the tidal fronts, then the impact on the seasonal stratification could be larger and the impact on the ecosystem larger still. Proposed wind farms around the UK include an extension to the wind farm which straddles the tidal front between the Isle of Man and the western English coast ("Walney exten-

sion"), a development which is likely to increase the impact on the stratification and thus the ecosystem dynamics. Larger OWFs off the east coast of Northern Ireland ("First Flight Wind"), in the eastern Irish Sea ("Celtic Array") and in the North Sea ("Dogger Bank" and "Hornsea") would fall within areas of significant seasonal stratification (Holt and Umlauf, 2008; Souza, 2013). The introduction of these structures within regions which are critical to the shelf ecosystem (Pingree et al., 1982; Richardson et al., 2000) may have impacts on resources within those areas e.g. fisheries, bird habitats (Miller and Christodoulou, 2014). Recent analyses of remotely sensed sea surface temperature shows the development of fronts is often associated with "charismatic megafauna" (Miller and Christodoulou, 2014). Thus, adding turbine monopiles can alter the structure of the fronts and impact on the migration of these megafauna. The knock on impacts from OWFs will be felt not only in the lower trophic levels (via stratification, mixing and nutrient cycling) but all the way to large marine vertebrates.

8. Conclusions

The use of a 3D unstructured hydrodynamic model of the coastal waters around the UK, forced with surface heat, tidal elevations and rivers, has, for the first time, modelled the impact at shelf sea scale of wind farm turbine monopiles. Model performance is validated against a large number of data sets (HF radar surface velocities and coastal and offshore surface elevation time series). The model results are analysed in terms of the impacts on the velocity fields (both horizontal and vertical), on the distribution of tidal constituents at near- and far-field scales, and on the vertical structure of the water column.

An analysis of the sensitivity of FVCOM to model processes in the immediate vicinity of the wind turbine monopiles is sensitive to the unstructured grid resolution, but that the sub-grid scale parameterisations in FVCOM underestimate those impacts. The magnitudes of the impacts presented here are between 65% and 80% of the values which might be obtained from a model in which the grid resolution at the turbine (2.5m) extends 150m from the monopile.

The introduction of turbine monopiles into the eastern Irish Sea has been shown to induce change across the model domain. At the individual turbine scale, a radius of horizontal impact on velocity (5% reduction of peak velocities) is found to extend approximately 1km from each turbine, or approximately 250 times the monopile diameter. Vertically, the turbines induce increased mixing of the water column due to flow up and down each monopile. Large-scale impacts from the turbines are felt all the way to the model boundaries and change the amplitude of the tides at the coasts in particular, but also offshore. In areas where seasonal stratification occurs, increased vertical transport induces greater mixing leading to a decrease in stratification. The horizontal extent of this disturbance is significantly larger than the sum of the footprint of the monopiles.

Whilst the modelling outlined here describes the first attempt at accurately scaled monopiles in a large-scale domain, it is not without its limitations. The performances of the sub-grid scale mixing parameterisations (Smagorinsky (1963) in the horizontal and GOTM with a k-ϵ formulation from Umlauf and Burchard (2005)) are pushed to their limits in the vicinity of the turbine monopiles. Whilst the grid sensitivity analysis has shown that the resolution used in the shelf model is an underestimate of the impacts generated from higher resolution grids, a non-hydrostatic FVCOM model configuration could overcome some of these limitations. However, given the already onerous computational requirements, it may not yet be practical to perform this work. There is also proof-of-concept work in which FVCOM is coupled with a CFD model (Wu and Tang, 2010), which would be an alternative route of investigation, although it is also not without significant challenges.

When considering future offshore wind farms, this work highlights the importance of their placement on impacts onshore (e.g. flooding, visual, noise), in intertidal areas (e.g. bird habitats) and offshore (e.g. nutrient cycling through seasonal mixing), particularly when

candidate sites are subject to seasonal stratification. This is particularly important given the future expansion of the UK's offshore wind farms and the proposed locations of the next round of construction, which includes some large offshore wind farms in areas of significant stratification close to the coast.

9. Acknowledgements

The work was supported by the UK Energy Research Centre (UKERC) Energy & Environment Phase II project and NERC/DEFRA FLOWBEC (NE/J004316/1). J. I. Allen was supported by NERC National Capability funding. FVCOM was run on the NERC HPC facility (ARCHER). The National Oceanography Centre Liverpool Bay Coastal Observatory (CObs) (http://cobs.noc.ac.uk) provided HF radar data, Liverpool Bay high resolution bathymetry and POLCOMS HRCS domain bathymetry. Tide gauge data supplied by the National Tidal and Sea Level Facility (NTSLF) via the British Oceanographic Data Centre (BODC). Bottom pressure sensor data was downloaded from the BODC. HF radar data from the PRIMaRE project kindly supplied by Daniel Conley at the University of Plymouth. Surface forcing data were obtained from the National Centers for Environmental Prediction and Department of Energy Atmospheric Model Intercomparison Project (NCEP-DOE AMIP-II) Reanalysis-2 heat flux data. Precipitation and evaporation were obtained from the Met Office Unified Model (MetUM) via the British Atmospheric Data Centre (BADC). River temperature data for England were obtained from the Environment Agency Freshwater River Temperature Archive. Figures were plotted using Python matplotlib (Hunter, 2007). Colour maps used are those from the matplotlib cmocean package by Kristen Thyng.

10. References

Adams, T., Black, K., MacIntyre, C., MacIntyre, I., and Dean, R. (2012). Connectivity modelling and network analysis of sea lice infection in Loch Fyne, west coast of Scotland. *Aquaculture Environment Interactions*, 3(1):51–63.

Adams, T. P., Miller, R. G., Aleynik, D., and Burrows, M. T. (2014). Offshore marine renewable energy devices as stepping stones across biogeographical boundaries. *Journal of Applied Ecology*, 51(2):330–338.

Andersen, O. B. (1995). Global ocean tides from ERS 1 and TOPEX/POSEIDON altimetry. *Journal of Geophysical Research*, 100(C12):25249–25.

Artioli, Y., Blackford, J. C., Butenschön, M., Holt, J. T., Wakelin, S. L., Thomas, H., Borges, A. V., and Allen, J. I. (2012). The carbonate system in the North Sea: Sensitivity and model validation. *Journal of Marine Systems*, 102-104:1–13.

Barange, M., Allen, I., Allison, E., Badjeck, M.-C., Blanchard, J., Drakeford, B., Dulvy, N. K., Harle, J., Holmes, R., Holt, J., Jennings, S., Lowe, J., Merino, G., Mullon, C., Pilling, G., Rodwell, L., Tompkins, E., and Werner, F. (2011). Predicting the Impacts and Socio-Economic Consequences of Climate Change on Global Marine Ecosystems and Fisheries. In *World Fisheries: A Social-Ecological Analysis*, pages 29–59. Wiley-Blackwell.

Bartlett, J. M. (1998). Quality Control Manual for Computational Estuarine Modelling. Technical Report 5, Environment Agency, Bristol.

Blackford, J., Torres, R., Cazanave, P., and Artioli, Y. (2013). Modelling Dispersion of CO2 Plumes in Sea Water as an Aid to Monitoring and Understanding Ecological Impact. *Energy Procedia*, 37:3379–3386.

Bleck, R. (2002). An oceanic general circulation model framed in hybrid isopycnic-Cartesian coordinates. *Ocean modelling*, 4(1):55–88.

Bleck, R. and Boudra, D. B. (1981). Initial Testing of a Numerical Ocean Circulation Model Using a Hybrid (Quasi-Isopycnic) Vertical Coordinate. *Journal of Physical Oceanography*, 11(6):755–770.

Blumberg, A. F. and Kantha, L. H. (1985). Open Boundary Condition for Circulation Models. *Journal of Hydraulic Engineering*, 111(2):237–255.

Bowers, D. G. and Simpson, J. H. (1987). Mean position of tidal fronts in European-shelf seas. *Continental Shelf Research*, 7(1):35–44.

Carbon Trust (2008). Offshore wind power: big challenge, big opportunity - Maximising the environmental, economic and security benefits. Technical report, Carbon Trust.

Chen, C., Beardsley, R. C., Cowles, G., Qi, J., Lai, Z., Gao, G., Stuebe, D., Xu, Q., Xue, P., Ge, J., Hu, S., Ji, R., Tian, R. C., Huang, H., Wu, L., Lin, H., Sun, Y., and Zhao, L. (2013). An Unstructured Grid, Finite-Volume Community Ocean Model: FVCOM User Manual.

Chen, C., Huang, H., Beardsley, R. C., Liu, H., Xu, Q., and Cowles, G. (2007). A finite volume numerical approach for coastal ocean circulation studies: Comparisons with finite difference models. *Journal of Geophysical Research*, 112(C3).

Chen, C., Liu, H., and Beardsley, R. C. (2003). An Unstructured Grid, Finite-Volume, Three-Dimensional, Primitive Equations Ocean Model: Application to Coastal Ocean and Estuaries. *Journal of*

Atmospheric and Oceanic Technology, 20(1):159–186.

Christiansen, M. B. and Hasager, C. B. (2005). Wake effects of large offshore wind farms identified from satellite SAR. *Remote Sensing of Environment*, 98(2-3):251–268.

Christie, E., Li, M., and Moulinec, C. (2012). Comparison of 2D and 3D large scale morphological modeling of offshore wind farms using HPC. In *Coastal Engineering Proceedings*, volume 33.

Cloet, R. L. (1954). Hydrographic Analysis of the Goodwin Sands and the Brake Bank. *The Geographical Journal*, 120(2):203.

Codiga, D. L. (2011). *Unified tidal analysis and prediction using the UTide Matlab functions*. Graduate School of Oceanography, University of Rhode Island.

Davies, A. M. and Jones, J. E. (1996). Sensitivity of tidal bed stress distributions, near-bed currents, overtides, and tidal residuals to frictional effects in the eastern Irish Sea. *Journal of Physical Oceanography*, 26(12):2553–2575.

Donnelly, C., Rosberg, J., and Isberg, K. (2012). A validation of river routing networks for catchment modelling from small to large scales. *Hydrology Research*, 44(5):917–925.

Doodson, A. T. and Corkan, R. H. (1933). The Principal Constituent of the Tides in the English and Irish Channels. *Philosophical Transactions of the Royal Society of London*, 231:29–53.

Egbert, G. D., Bennett, A. F., and Foreman, M. G. G. (1994). TOPEX/POSEIDON tides estimated using a global inverse model. *Journal of Geophysical Research*, 99(C12):24821–24852.

Egbert, G. D. and Erofeeva, S. Y. (2002). Efficient Inverse Modeling of Barotropic Ocean Tides. *Journal of Atmospheric and Oceanic Technology*, 19(2):183–204.

Egbert, G. D., Erofeeva, S. Y., and Ray, R. D. (2010). Assimilation of altimetry data for nonlinear shallow-water tides: Quarter-diurnal tides of the Northwest European Shelf. *Continental Shelf Research*, 30(6):668–679.

Fairall, C. W., Bradley, E. F., Hare, J. E., Grachev, A. A., and Edson, J. B. (2003). Bulk parameterization of air-sea fluxes: Updates and verification for the COARE algorithm. *Journal of Climate*, 16(4):571–591.

Hasager, C., Rasmussen, L., Peña, A., Jensen, L., and Réthoré, P.-E. (2013). Wind Farm Wake: The Horns Rev Photo Case. *Energies*, 6(2):696–716.

Holt, J., Butenschön, M., Wakelin, S. L., Artioli, Y., and Allen, J. I. (2012). Oceanic controls on the primary production of the north-west European continental shelf: model experiments under recent past conditions and a potential future scenario. *Biogeosciences*, 9(1):97–117.

Holt, J. and Umlauf, L. (2008). Modelling the tidal mixing fronts and seasonal stratification of the Northwest European Continental shelf. *Continental Shelf Research*, 28(7):887–903.

Howarth, M., Player, R., Wolf, J., and Siddons, L. (2007). HF radar measurements in Liverpool Bay, Irish Sea. In *OCEANS 2007 - Europe*, pages 1–6.

Huang, H. (2011). Finite volume coastal ocean model (FVCOM) 3D hydrodynamic model comparison. Technical report, Louisiana State University, Department of Oceanography and Coastal Sciences.

Hunter, J. (May-June 2007). Matplotlib: A 2D Graphics Environment. *Computing in Science & Engineering*, 9(3):90–95.

Jensen, M. S., Larsen, B. J., Frigaard, P., Vos, L. D., Christensen, E. D., Hansen, E. A., Solberg, T., Hjertager, B. H., and Bove, S. (2006). Offshore Wind Turbines situated in Areas with Strong Currents. Consortium report 6004RE01ER1, Rambøll, Aalborg Universitet, Offshore Center Danmark.

Jones, J. E. and Davies, A. M. (2007a). A high-resolution finite element model of the M2, M4, M6, S2, N2, K1 and O1 tides off the west coast of Britain. *Ocean Modelling*, 19(1-2):70–100.

Jones, J. E. and Davies, A. M. (2007b). On the sensitivity of tidal residuals off the west coast of Britain to mesh resolution. *Continental Shelf Research*, 27(1):64–81.

Jones, J. E., Hall, P., and Davies, A. M. (2009). An inter-comparison of tidal solutions computed with a range of unstructured grid models of the Irish and Celtic Sea Regions. *Ocean Dynamics*, 59(6):997–1023.

Kanamitsu, M., Ebisuzaki, W., Woollen, J., Yang, S.-K., Hnilo, J. J., Fiorino, M., and Potter, G. L. (2002). NCEP-DOE AMIP-II Reanalysis (R-2). *Bulletin of the American Meteorological Society*, 83(11):1631–1643.

Lambkin, D. O., Harris, J. M., Cooper, W. S., and Coates, T. (2009). Coastal Process Modelling for Offshore Wind Farm Environmental Impact Assessment: Best Practice Guide. Technical report, COWRIE.

Legrand, S., Deleersnijder, E., Delhez, E., and Legat, V. (2007). Unstructured, anisotropic mesh generation for the Northwestern European continental shelf, the continental slope and the neighbouring ocean. *Continental Shelf Research*, 27(9):1344–1356.

Li, X., Chi, L., Chen, X., Ren, Y., and Lehner, S. (2014). SAR observation and numerical modeling of tidal current wakes at the East China Sea offshore wind farm. *Journal of Geophysical Research: Oceans*, 119(8):4958–4971.

Ludewig, E. (2015). *On the Effect of Offshore Wind Farms on the Atmosphere and Ocean Dynamics*, volume 31 of *Hamburg Studies on Maritime Affairs*. Springer International Publishing, Cham.

Martin-Short, R., Hill, J., Kramer, S., Avdis, A., Allison, P., and Piggott, M. (2015). Tidal resource extraction in the Pentland Firth, UK: Potential impacts on flow regime and sediment transport in the Inner Sound of Stroma. *Renewable Energy*, 76:596–607.

Melville, B. W. and Sutherland, A. J. (1989). Design Method for Local Scour at Bridge Piers. *Journal of Hydraulic Engineering*, 114(10):1210–1226.

Miller, P. I. and Christodoulou, S. (2014). Frequent locations of oceanic fronts as an indicator of pelagic diversity: Application to marine protected areas and renewables. *Marine Policy*, 45:318–329.

MRG Consulting Engineers Limited (2013). Dublin Array - An Offshore Wind Farm on the Kish and Bray Banks - Environmental Impact Statement Addendum Appendix B. Environmental Impact

Statement HEL095501, MRG Consulting Engineers Limited.

Okorie, O. P. (2011). *Scale effects in testing of a monopile support structure submerged in tidal currents*. PhD thesis, Robert Gordon University.

Orr, H. G., des Clers, S., Simpson, G. L., Hughes, M., Battarbee, R. W., Cooper, L., Dunbar, M. J., Evans, R., Hannaford, J., Hannah, D. M., Laize, C., Richards, K. S., Watts, G., and Wilby, R. L. (2010). Changing water temperatures: a surface water archive for England and Wales. In Kirby, C., editor, *Role of Hydrology in Managing Consequences of a Changing Global Environment*. British Hydrological Society.

Palmer, M. R. (2010). The modification of current ellipses by stratification in the Liverpool Bay ROFI. *Ocean Dynamics*, 60(2):219–226.

Pelling, H. E., Green, J. A. M., and Ward, S. L. (2013). Modelling tides and sea-level rise: To flood or not to flood. *Ocean Modelling*, 63(December 2012):21–29.

Pickering, M., Wells, N., Horsburgh, K., and Green, J. (2012). The impact of future sea-level rise on the European Shelf tides. *Continental Shelf Research*, 35:1–15.

Pingree, R. D. and Maddock, L. (1977). Tidal residuals in the English Channel. *Journal of the Marine Biological Association of the United Kingdom*, 57(02):339–354.

Pingree, R. D., Mardell, G. T., Holligan, P. M., Griffiths, D. K., and Smithers, J. (1982). Celtic Sea and Armorican current structure and the vertical distributions of temperature and chlorophyll. *Continental Shelf Research*, 1(1):99–116.

Proctor, R., Holt, J., Allen, J., and Blackford, J. (2003). Nutrient fluxes and budgets for the North West European Shelf from a three-dimensional model. *The Science of The Total Environment*, 314-316:769–785.

Proudman, J. and Doodson, A. T. (1924). The Principal Constituent of the Tides of the North Sea. *Philosophical Transactions of the Royal Society of London. Series A, Containing Papers of a Mathematical or Physical Character*, 224(616-625):185–219.

Rennau, H., Schimmels, S., and Burchard, H. (2012). On the effect of structure-induced resistance and mixing on inflows into the Baltic Sea: A numerical model study. *Coastal Engineering*, 60:53–68.

Richardson, K., Visser, A. W., and Pedersen, F. B. (2000). Subsurface phytoplankton blooms fuel pelagic production in the North Sea. *Journal of Plankton Research*, 22(9):1663–1671.

Robinson, A. M. and Wyatt, L. R. (2011). A two year comparison between HF radar and ADCP current measurements in Liverpool Bay. *Journal of operational oceanography*, 4(1):33–45.

Robinson, A. M., Wyatt, L. R., and Howarth, M. J. (2013). HF Radar data availability and measurement accuracy in Liverpool Bay before and after the construction of Rhyl-Flats wind farm. *Journal of Operational Oceanography*, 6(2):1–12.

Roulund, A., Sumer, B. M., Fredsøe, J., and Michelsen, J. (2005). Numerical and experimental investigation of flow and scour around a circular pile. *Journal of Fluid Mechanics*, 534:351–401.

Serhadlıoğlu, S., Adcock, T. A., Houlsby, G. T., Draper, S., and Borthwick, A. G. (2013). Tidal stream energy resource assessment of the Anglesey Skerries. *International Journal of Marine Energy*, 3-4:e98–e111.

Shapiro, G. I. (2011). Effect of tidal stream power generation on the region-wide circulation in a shallow sea. *Ocean Science*, 7(1):165–174.

Simpson, J. H., Brown, J., Matthews, J., and Allen, G. (1990). Tidal straining, density currents, and stirring in the control of estuarine stratification. *Estuaries*, 13(2):125–132.

Simpson, J. H. and Hunter, J. R. (1974). Fronts in the Irish sea. *Nature*, 250:404–406.

Smagorinsky, J. (1963). General Circulation experiments with the primitive equations I. The basic experiment. *Monthly Weather Review*, 91(3):99–164.

Smyth, T. J., Allen, I., Atkinson, A., Bruun, J. T., Harmer, R. A., Pingree, R. D., Widdicombe, C. E., and Somerfield, P. J. (2014). Ocean Net Heat Flux Influences Seasonal to Interannual Patterns of Plankton Abundance. *PLoS ONE*, 9(6):e98709.

Souza, A. J. (2013). On the use of the Stokes number to explain frictional tidal dynamics and water column structure in shelf seas. *Ocean Science*, 9(2):391–398.

Souza, A. J. and Simpson, J. H. (1996). The modification of tidal ellipses by stratification in the Rhine ROFI. *Continental Shelf Research*, 16(8):997–1007.

Torres, R. and Uncles, R. J. (2011). Modeling of Estuarine and Coastal Waters. In *Modeling of Estuarine and Coastal Waters*, volume 2 of *Treatise on Estuarine and Coastal Science*. Elsevier.

Umlauf, L. and Burchard, H. (2005). Second-order turbulence closure models for geophysical boundary layers. A review of recent work. *Continental Shelf Research*, 25(7-8):795–827.

van der Molen, J., Smith, H. C., Lepper, P., Limpenny, S., and Rees, J. (2014). Predicting the large-scale consequences of offshore wind turbine array development on a North Sea ecosystem. *Continental Shelf Research*, 85:60–72.

Vanhellemont, Q. and Ruddick, K. (2014). Turbid wakes associated with offshore wind turbines observed with Landsat 8. *Remote Sensing of Environment*, 145:105–115.

Waggitt, J., Cazenave, P., Torres, R., Williamson, B., and Scott, B. (2016a). Predictable microhabitat use among deep-diving seabirds in a high energy environment. *ICES Journal of Marine Science*.

Waggitt, J. J., Cazenave, P. W., Torres, R., Williamson, B. J., and Scott, B. E. (2016b). Quantifying pursuit-diving seabirds' associations with fine-scale physical features in tidal stream environments. *Journal of Applied Ecology*, pages n/a–n/a.

Wakelin, S. L., Holt, J. T., Blackford, J. C., Allen, J. I., Butenschön, M., and Artioli, Y. (2012). Modeling the carbon fluxes of the northwest European continental shelf: Validation and budgets. *Journal of Geophysical Research*, 117(C5).

Wessel, P. and Smith, W. H. F. (1996). A global, self-consistent, hierarchical, high-resolution shoreline database. *Journal of Geophysical Research*, 101(B4):8741–8743.

Wu, X.-g. and Tang, H.-s. (2010). Coupling of CFD model and FV-

COM to predict small-scale coastal flows. *Journal of Hydrodynamics, Ser. B*, 22(5):284–289.

Yang, Z. and Khangaonkar, T. (2008). Modeling of salt intrusion, intertidal mixing, and circulation in a braided estuary. *Journal of Coastal Research*, pages 171–180.

Yang, Z., Wang, T., Copping, A., and Geerlofs, S. (2014). Modeling of in-stream tidal energy development and its potential effects in Tacoma Narrows, Washington, USA. *Ocean & Coastal Management*, 99:52–62.

Yang, Z., Wang, T., and Copping, A. E. (2013). Modeling tidal stream energy extraction and its effects on transport processes in a tidal channel and bay system using a three-dimensional coastal ocean model. *Renewable Energy*, 50:605–613.

Zheng, L. and Weisberg, R. H. (2012). Modeling the west Florida coastal ocean by downscaling from the deep ocean, across the continental shelf and into the estuaries. *Ocean Modelling*, 48:10–29.

Zhou, J., Pan, S., and Falconer, R. A. (2014). Effects of open boundary location on the far-field hydrodynamics of a Severn Barrage. *Ocean Modelling*, 73:19–29.